Continental Shelf Research 211 (2020) 104291

Contents lists available at ScienceDirect

Continental Shelf Research

journal homepage: http://www.elsevier.com/locate/csr

# Armoring and exposure effects on the wave-driven sediment transport

Yashar Rafati [a,*], Tian-Jian Hsu [a], Zhen Cheng [b], Xiao Yu [c], Joseph Calantoni [d]

[a] Center for Applied Coastal Research, Department of Civil and Environmental Engineering, University of Delaware, Newark, DE, 19716, USA
[b] Convergent Science, Inc., Madison, WI, 53719, USA
[c] Department of Civil and Coastal Engineering, University of Florida, Gainesville, FL, 32611, USA
[d] Ocean Sciences Division, U.S. Naval Research Laboratory, Stennis Space Center, MS, 39529, USA

ARTICLE INFO

*Keywords:*
Onshore sediment transport
Particle size distribution
Inverse vertical grading
Velocity/acceleration skewness
Exposure/armoring effect
Active layer

ABSTRACT

Coastal sediment transport of graded spherical particles with the material properties of sand was simulated and compared to transport of the uniform-sized spherical particles using a two-phase Eulerian-Lagrangian model. The fluid phase solver was based on SedFoam developed in OpenFOAM and the open-source discrete element method solver LIGGGHTS was used for the particle phase. We validated the model for sheet flow of well-sorted medium sand ($d_{50} = 0.28$ mm) and mixed sand with bimodal size distribution in velocity-skewed oscillatory flows as well as well-sorted coarse sand ($d_{50} = 0.51$ mm) in velocity-skewed and acceleration-skewed oscillatory flows. Simulation results of graded particles showed the formation of inverse grading (upward coarsening) in sediment bed under oscillatory flows, suggesting that the effects of armoring and exposure were important in the resulting transport rate. Examining different particle size distributions under onshore velocity-skewed flows, it was found that the largest increase of the net onshore sediment transport rate due to size gradation corresponded to the moderately sorted particle size distribution ($d_{90}/d_{10} = 3.41$), where the coarse fraction ($d > d_{50}$) had the maximum contribution to the transport. By analyzing intra-wave sediment transport quantities, the response of size gradation to the flow skewness and asymmetry and velocity intensity was investigated. Model results revealed that the armoring effect (reduction of sediment flux due to inverse grading) was dominant when flow velocity magnitude was lower (wave trough) or the fluid acceleration was higher. On the other hand, when flow velocity magnitude was larger (wave crest), the armoring effect was reduced or the exposure effect (enhancement of sediment flux due to inverse grading) may become more pronounced. Overall, we found that onshore net sediment transport was enhanced up to 30% due to particle size gradation under onshore velocity-skewed oscillatory flows. Conversely, the size gradation reduced the net onshore transport rate up to 35% under onshore acceleration-skewed oscillatory flows. Model results also suggested that the thickness of the active layer (surface layer affected by vertical sorting) in sheet flows can be quantified by the peak erosion depth. The simulation results presented here provide insights into the role of sediment size gradation (armoring and exposure effects) in wave-driven onshore transport which is important for predicting morphological evolution.

## 1. Introduction

Offshore/onshore sediment transport in the coastal environments, namely the cross-shore sediment transport process, is an important factor driving the morphological evolution of the coastal zones. In particular, the so-called sheet flow transport regime, in which the flow driving forces are intense such that a large amount of transport occurs in a concentrated layer over a predominantly flat bed, has been considered as a major mechanism driving cross-shore sediment transport in the nearshore (e.g., Nielsen, 1992). Onshore sediment transport is often associated with wave-induced velocity skewness and acceleration skewness. Seaward of wave breaking, the near-bed wave orbital velocity time series tends to be onshore skewed (high orbital velocity at the wave crest and low orbital velocity at the trough) due to the wave shoaling effect (Elfrink et al., 2006). Velocity skewness was found to be a dominant mechanism driving onshore transport and sandbar migration (Fernández-Mora et al., 2015; Hsu et al., 2006). As waves propagate toward the inner-surf zone, the wave orbital velocity is not only velocity-skewed but also acceleration-skewed (higher onshore flow acceleration), typically referred to as sawtooth shape of orbital velocity

* Corresponding author.
*E-mail address:* yashar@udel.edu (Y. Rafati).

https://doi.org/10.1016/j.csr.2020.104291
Received 17 August 2019; Received in revised form 18 October 2020; Accepted 25 October 2020
Available online 28 October 2020

time series. The resulting high onshore acceleration contributes to the wave-averaged onshore sediment transport (Drake and Calantoni, 2001; Nielsen, 2006) and may contribute to beach recovery (Hoefel and Elgar, 2003).

Understanding wave-driven sediment transport is fundamental to the improvement of regional-scale morphodynamic models (Roelvink et al., 2009; Warner et al., 2010). There have been many experimental and numerical investigations focused on the role of velocity and acceleration skewness on the sediment transport in the sheet flow regime (e.g., Van der A et al., 2010; Drake and Calantoni, 2001; Flores and Sleath, 1998; Hsu and Hanes, 2004; O'Donoghue and Wright, 2004a; Ribberink and Al-Salem, 1994; Watanabe and Sato, 2004). These studies revealed that the mechanisms of driving onshore sediment transport under waves with velocity and acceleration skewness are different. Under velocity-skewed waves, the onshore sediment transport is driven by the more energetic near-bed flow during the crest interval that causes deeper erosion of sediment bed along with more significant sediment suspension (O'Donoghue and Wright, 2004a). Under acceleration-skewed waves, the premature development of the wave boundary layer during the onshore acceleration period was found to generate a greater amount of bed shear stress which leads to higher sediment entrainment during the crest interval (Abreu et al., 2013; Nielsen, 2006). The other mechanism for onshore transport driven by the acceleration-skewed waves is the momentary bed failure (Madsen, 1974) or plug flow (Flores and Sleath, 1998) generated by the high horizontal pressure gradient due to significant onshore flow acceleration. Onshore sediment transport under surface waves is also attributed to the progressive wave streaming effect which interacts with velocity and acceleration skewness (e.g, Kim et al., 2018; Kranenburg et al., 2013).

Along with the hydrodynamic factors, sediment characteristics also play an important role in transport processes (e.g., Holland and Elmore, 2008). Density, size and shape are some of the important properties that affect the mobility, suspension and transport of sediment. Sediment particles are rarely of uniform size in the coastal zones and the key issue is to quantify the effects of sediment size gradation on shaping coastal morphology. Due to size-selective transport of sediment in the coastal environments, size gradation causes notable sorting in the horizontal (cross-shore) and vertical directions (Goff et al., 2005; Schwartz and Birkemeier, 2004; Wiberg et al., 1994). A key factor controlling size sorting is the local particle size distribution. The size distributions may be classified from very well-sorted with narrow size distribution to very poorly-sorted with wide size distribution (Folk and Ward, 1957). Based on field measurements in Duck, NC, USA, the median grain diameter of sand in the dune face was about 0.5 mm, but it decreased to about 0.15 mm in the most offshore gauge at 8 m water depth (Stauble, 1992). Furthermore, Stauble (1992) observed poorly-sorted sand in the dune face and at the berm with a narrowing trend in offshore direction, where the sand grains became well-sorted in the offshore gauges deeper than about 6 m. The trend of more well-sorted sand in the offshore direction was attributed to the diminishing wave energy intensity.

Vertical sorting of sediment grains in the coastal zones has caught researchers' attention. Under wave action, the vertical sorting is known as the inverse grading, which describes finer (coarser) sand particles migrate downward (upward) (Calantoni and Thaxton, 2008; Harada et al., 2015; Hassan and Ribberink, 2005; Lyne et al., 1990). In steady flows, Julien et al. (1993) also reported finer grains settle more easily and migrate to deeper layers while the coarse grains are more exposed on the bed surface. This inverse grading is also known as kinematic sorting. From the kinematic energy point of view, due to the collision of fine and coarse particles, the relative kinematic energy loss of fine fractions is more significant compared to coarse fractions. Inverse grading has also been observed in granular segregation known as Brazil Nut effect (Rosato et al., 1987). From this point of view, during the shaking of a granular bed, the generated voids beneath the coarse particles are more probable to be filled with fine particles. As this process continues, the coarse particles migrate upward and become exposed and the fine particles migrate downward and get armored by the coarse particles.

Only a handful of studies focused on transport rate and critical shear stress of graded sediments under steady and oscillatory flow conditions (Dibajnia and Watanabe, 1996; Hassan and Ribberink, 2005; Kleinhans and van Rijn, 2002; Sistermans, 2002). Due to vertical sorting of sediment particles, the coarse particles exposed on the bed surface have a higher chance of getting entrained, while the fine particles armored in deeper bed layers have a weaker contribution to the transported sediment. As a result, transport in graded sediments can be dominated by the coarse particles. These processes are referred to as exposure and armoring effects in the literature (Van Rijn, 2007; Wiberg et al., 1994). The parameterizations proposed to incorporate the effect of armoring and exposure are mainly based on two approaches (Van Rijn, 2007). The first approach focuses on the incipient motion of each grain size fraction, where the more exposed coarse fractions require relatively lower shear stress to get mobilized, while relatively higher shear stress is needed to mobilize the fine fractions armored in deeper bed layers. The second approach estimates the effective (nondimensional) bed shear stress on each size fraction, where the exposed coarse fractions get higher bed shear stress, while the armored fine fractions receive lower bed shear stress due to being shielded by coarse grains. The latter approach was implemented in the recent sand transport formula by Van der A et al. (2013). Although these existing studies shed lights on the key mechanisms affecting transport of graded sediments, the effect of wave shape and wave intensity on the degree of armoring and exposure effects and the resulting transport was not fully understood. As the wave shape and intensity in the coastal environments are of significant variety, a great attention is required to investigate the effect of these variabilities on the sediment transport processes.

In the past two decades, Eulerian-Lagrangian models, namely a discrete element method (DEM) coupled with a fluid solver, have been utilized to simulate sediment transport processes under steady and oscillatory flows in order to better capture the fluid-particle and particle-particle interaction in sediment transport (e.g., Cheng et al., 2018; Drake and Calantoni, 2001; Finn et al., 2016; Schmeeckle, 2014; Sun and Xiao, 2016). Polydisperse sediment particles and non-spherical grain shapes are the features that can also be studied using DEM (Calantoni et al., 2004; Calantoni and Thaxton, 2008; Harada et al., 2015; Sun et al., 2017). More recently, 3D large-eddy simulation (LES) fluid solvers are coupled with DEM to investigate the interactions between fluid turbulence and sediment particles in transport (Finn et al., 2016; Liu et al., 2018; Schmeeckle, 2014).

The purpose of this study is to understand the effect of armoring and exposure of graded sand bed during sheet flow sediment transport driven by different wave shapes and wave intensities for a range of grain size distribution. At the moment, an extensive numerical study of wave-driven sediment transport over a wide range of wave conditions and grain size distributions using a turbulence-resolving LES approach would require exhaustive computational resources. Alternatively, a turbulence-averaged approach based on solving the Eulerian two-phase equations with a two-equation closure on the turbulence and turbulence-sediment interactions has been shown to be promising in modeling sheet flow sediment transport in the wave bottom boundary layers (e.g., Amoudry and Liu, 2010; Cheng et al., 2017). In this study, we extended an Eulerian-Lagrangian turbulence-averaged two-phase flow model reported by Cheng et al. (2018) to simulate wave-driven sheet flows. To simulate the turbulence-induced particle suspension, Cheng et al. (2018) implemented an eddy interaction model (Graham and James, 1996), which incorporates the instantaneous fluid velocity fluctuations in the drag force formulation. In Cheng et al. (2018), the numerical model was calibrated and validated for sediment transport in steady channel flows. Hence, the present study will first validate the model for oscillatory sheet flow and then investigate size grading effects on wave-driven sheet flow. The numerical simulations for

wave-averaged sediment transport rates were also compared with a comprehensive parameterization reported by Van der A et al. (2013), which takes different characteristic of waves along with sediment properties into account, including the effect of size gradation.

Although it is well-established that wave skewness and asymmetry drive onshore sediment transport in the nearshore, how the corresponding armoring and exposure effects due to size gradation can influence the onshore transport rate has not been quantified. To achieve this research objective, we made the effort to simulate the near-bed flow conditions similar to typical moderate to high-energy incoming waves landward from the wave shoaling zone through the inner surf zone. Accordingly, simulations were carried out for different wave shapes and wave intensities and for bed sediment composed of uniform-sized and graded particles with different size distribution. The remaining manuscript is organized as follows. The mathematical formulation of the Eulerian-Lagrangian numerical model and the Van der A et al. (2013) parameterization are summarized in Section 2. Section 3 reports the validation of Eulerian-Lagrangian model for oscillatory sheet flows. Section 4 is devoted to the investigation of grading effects on sheet flow transport subjected to oscillatory flow velocity shapes and velocity intensities. A discussion on erosion depth and active layer thickness due to grading effect is presented in Section 5. Concluding remarks are given in Section 6.

## 2. Methods

### 2.1. Eulerian-Lagrangian model

The Eulerian-Lagrangian model adopted in this study incorporates the fluid phase of the open-source solver SedFoam (Cheng et al., 2017), which is an Eulerian two-phase model for sediment transport created using OpenFOAM. For the Lagrangian particle phase, the open-source solver LIGGGHTS (Kloss et al., 2012) based on discrete element method (DEM) is used. The coupling of these two solvers is achieved with another open-source code CFDEM (Goniva et al., 2012). More detailed discussion on model formulation and numerical scheme can be found in Cheng et al. (2018).

The position of each particle is tracked by solving the translational and rotational equations of motion, respectively,

$$m_i\frac{d\boldsymbol{v}_i}{dt}=\boldsymbol{f}_{d,i}+\left(\boldsymbol{f}_{x,i}-\nabla_i p\right)\cdot V_i+\sum_{j=1}^{N_c}\left(\boldsymbol{f}_{n,ij}+\boldsymbol{f}_{t,ij}\right)+m_i\boldsymbol{g}, \tag{1}$$

$$I_i\frac{d\Omega_i}{dt}=\sum_{j=1}^{N_c}\left(\boldsymbol{M}_{t,ij}+\boldsymbol{M}_{r,ij}\right), \tag{2}$$

where $\boldsymbol{v}_i$is the translational velocity of particle, $\boldsymbol{f}_{d,i}$is the drag force acting on particle $i$, $\boldsymbol{f}_{x,i}$is the external body force driving the oscillatory flow, $\nabla_i p$is the fluid pressure gradient interpolated at particle $i$, and $V_i$is the volume of particle $i$. The normal and tangential contact forces on particle $i$from particle $j$are expressed as $\boldsymbol{f}_{n,ij}$and $\boldsymbol{f}_{t,ij}$, respectively, with $N_c$the number of particles in contact with particle $i$, and $m_i\boldsymbol{g}$is the gravitational force. In (2), $I_i$ and $\Omega_i$ are the moment of inertia and the angular velocity of particle $i$, respectively, $\boldsymbol{M}_{t,ij}$is the torque generated by the tangential force and $\boldsymbol{M}_{r,ij}$is known as rolling friction torque (Luding, 2008). The formulation of the drag force will be discussed below.

The soft sphere model (Cundall and Strack, 1979) calculates the intergranular forces based on Hertzian contact theory, where the normal forces are estimated as a nonlinear function of the overlap generated between two colliding spheres. In this study, we used an improved soft sphere model, which also incorporates the energy dissipation in compression and restitution stages of collision, along with the estimation of tangential forces based on Hertz-Mindlin contact model (Machado et al., 2012). The same set of coefficients as specified by Cheng et al. (2018) were used in the present DEM model including the Young's modulus as $E = 5\times 10^6$Pa, the restitution coefficient as $e = 0.5$, the Coulomb friction coefficient as $\mu_c = 0.5$, and the Poisson's ratio as $e = 0.45$. Previous results show sediment transport rates are largely insensitive to the precise choice of DEM coefficients (e.g., Drake and Calantoni, 2001).

The fluid phase is solved based on the Reynolds-averaged momentum equation,

$$\frac{\partial\rho_f\left(1-\overline{\varphi}_s\right)\overline{\boldsymbol{u}}_f}{\partial t}+\nabla\cdot\left[\rho_f\left(1-\overline{\varphi}_s\right)\overline{\boldsymbol{u}}_f\overline{\boldsymbol{u}}_f\right]=\left(1-\overline{\varphi}_s\right)\boldsymbol{f}_x-\left(1-\overline{\varphi}_s\right)\nabla\overline{p}+\nabla\cdot\boldsymbol{\tau}_f+\rho_f\left(1-\overline{\varphi}_s\right)\boldsymbol{g}+\overline{\boldsymbol{F}}_d, \tag{3}$$

where the overbar denotes the ensemble-average operator, $\rho_f$is the fluid density, $\overline{\boldsymbol{u}}_f$ is the fluid velocity, $\overline{\varphi}_s$is the sediment concentration, $\overline{\boldsymbol{F}}_d$is the drag force of particles averaged in a fluid cell, and $\boldsymbol{\tau}_f$is the total fluid stress tensor. The total fluid stress tensor is the sum of viscous stress ($\boldsymbol{\tau}_v$) and Reynolds stress ($\boldsymbol{\tau}_{ft}$), respectively,

$$\boldsymbol{\tau}_v=\rho_f\nu_f\left(1-\overline{\varphi}_s\right)\left(\nabla\overline{\boldsymbol{u}}_f+\nabla^T\overline{\boldsymbol{u}}_f-\frac{2}{3}\boldsymbol{I}\nabla\cdot\overline{\boldsymbol{u}}_f\right), \tag{4}$$

$$\boldsymbol{\tau}_{ft}=\rho_f\left(1-\overline{\varphi}_s\right)\left[\nu_{ft}\left(\nabla\overline{\boldsymbol{u}}_f+\nabla^T\overline{\boldsymbol{u}}_f-\frac{2}{3}\boldsymbol{I}\nabla\cdot\overline{\boldsymbol{u}}_f\right)-\frac{2}{3}k_f\boldsymbol{I}\right], \tag{5}$$

where $\nu_f$is the fluid kinematic viscosity, $\boldsymbol{I}$is the identity matrix, and $k_f$is the turbulent kinetic energy (TKE). $\nu_{ft}$is the turbulent eddy viscosity, which is calculated using the turbulent kinetic energy and the turbulent dissipation rate ($\varepsilon_f$),

$$\nu_{ft}=C_\mu\frac{\left(k_f\right)^2}{\varepsilon_f}, \tag{6}$$

where $C_\mu$is an empirical coefficient set to 0.09.

Turbulent kinetic energy and turbulent dissipation rate are calculated using a modified k-ε model for two-phase flow similar to Cheng et al. (2017). The transport equations for $k_f$and $\varepsilon_f$are written as,

$$\frac{\partial k_f}{\partial t}+\overline{\boldsymbol{u}}_f.\nabla k_f=\frac{\boldsymbol{\tau}_{ft}}{\rho_f}:\nabla\overline{\mathbf{u}}_f+\nabla\cdot\left[\left(\nu_f+\frac{\nu_{ft}}{\sigma_k}\right)\nabla k_f\right]-\varepsilon_f-\frac{2\beta(1-\lambda)\overline{\varphi}_s k_f}{\rho_f\left(1-\overline{\varphi}_s\right)}-\frac{1}{\left(1-\overline{\varphi}_s\right)}\frac{\nu_{ft}}{\sigma_c}(s-1)\boldsymbol{g}\cdot\nabla\overline{\varphi}_s, \tag{7}$$

$$\frac{\partial\varepsilon_f}{\partial t}+\overline{\boldsymbol{u}}_f\cdot\nabla\varepsilon_f=C_{1\varepsilon}\frac{\varepsilon_f}{k_f}\frac{\boldsymbol{\tau}_{ft}}{\rho_f}:\nabla\overline{\mathbf{u}}_f+\nabla\cdot\left[\left(\nu_f+\frac{\nu_{ft}}{\sigma_\varepsilon}\right)\nabla\varepsilon_f\right]-C_{2\varepsilon}\frac{\varepsilon_f}{k_f}\varepsilon_f-C_{3\varepsilon}\frac{\varepsilon_f}{k_f}\frac{2\beta(1-\lambda)\overline{\varphi}_s k_f}{\rho_f\left(1-\overline{\varphi}_s\right)}-C_{4\varepsilon}\frac{\varepsilon_f}{k_f}\frac{1}{\left(1-\overline{\varphi}_s\right)}\frac{\nu_{ft}}{\sigma_c}(s-1)\boldsymbol{g}\cdot\nabla\overline{\varphi}_s, \tag{8}$$

where ':' stands for the tensor contraction. The last two terms on the RHS of (7) and (8) quantify the turbulence attenuation by particle phase due to drag and buoyancy. $\lambda$is a parameter to quantify the correlation of sediment particle velocity fluctuations to the fluid velocity fluctuations (Cheng et al., 2017), which was proposed to be calculated as $\lambda = e^{-B.St}$, where $St$is the particle Stokes number and $B = 0.22$ is an empirical coefficient. The particle Stokes number is calculated as $St = t_p/t_l$(Balachandar and Eaton, 2010), where $t_p$is the particle response time and $t_l$is the characteristic time scale of energetic eddies. The values of empirical coefficients of the balance equations of $k_f$and $\varepsilon_f$used in the model are

shown in Table 1.

The drag force term on the RHS of (1) is calculated by averaging the particle drag forces within a fluid grid cell,

$$\overline{\boldsymbol{F}}_d = -\frac{1}{N_s V_{cell}} \sum_{j=1}^{N_s} \sum_{i=1}^{N_{cell}} \boldsymbol{f}_{d,i}, \tag{9}$$

where $V_{cell}$ is the volume of a fluid cell, $N_{cell}$ is the number of particles within a fluid cell, and $N_s$ is the number of DEM time steps within one CFD time step. The drag force on each particle is calculated as,

$$\boldsymbol{f}_{d,i} = \frac{1}{2} C_D A_{s,i} \left| \boldsymbol{u}_{f,i} - \boldsymbol{v}_{f,i} \right| \left( \boldsymbol{u}_{f,i} - \boldsymbol{v}_{f,i} \right), \tag{10}$$

where $C_D$is the drag coefficient (Haider and Levenspiel, 1989), $A_{s,i}$is the projected area of particle $i$, and $\boldsymbol{u}_{f,i}$is the instantaneous fluid velocity at the location of particle $i$. A closure model is needed to estimate the instantaneous fluid velocity fluctuations which particle suspension due to turbulence is based upon. The eddy-interaction model (Graham and James, 1996) has been demonstrated to have the capability of modeling turbulent suspension in steady sheet flow (Cheng et al., 2018), and we extended the model application for sheet flow under wave motion. In this model, the velocity fluctuations are calculated using Gaussian random numbers ($\sigma_1$, $\sigma_2$and$\sigma_3$, all having zero mean and standard deviation of 1) and turbulent kinetic energy, $k_{f,i}$, interpolated at the location of the particle $i$, as $\boldsymbol{u}'_{f,i} = \sqrt{2k_{f,i}/3}\sigma_1$, $\boldsymbol{v}'_{f,i} = \sqrt{2k_{f,i}/3}\sigma_2$, $\boldsymbol{w}'_{f,i} = \sqrt{2k_{f,i}/3}\sigma_3$. Once generated, these Gaussian random numbers remain constant during an eddy interaction life time, which is estimated as,

$$t_{e,i} = -C_0 \ln(1-\xi) T_{l,i}, \tag{11}$$

where $\xi$is a random number between 0 and 1, $T_{l,i}$is the mean eddy life time, estimated as $T_{l,i} = 0.165 k_{f,i}/\varepsilon_{f,i}$, and $C_0$is a coefficient calibrated to be 2.0 for the present simulations.

### 2.2. *Van der A et al. (2013) parameterization*

The practical sand transport formula developed by Van der A et al. (2013) aims at predicting the sediment transport driven by waves and currents. This formulation is calibrated using extensive laboratory data of oscillatory flow tunnels and large wave flumes. Most importantly, Van der A et al. (2013) formulation calculates the wave-averaged sediment transport rate based on parametrizing the bed shear stress incorporating the effect of wave shape (i.e. velocity and acceleration asymmetry), wave and current intensity, and progressive wave streaming. The formula covers a wide range of grain sizes as it also incorporates the effect of phase lag between the flow velocity and sediment entrainment important for finer sand ($d_{50} < 0.2$ mm). More detailed discussion on the parameterization can be found in Van der A et al. (2013). Here, we focus on its formulation for graded sand transport, which is an extension of the model proposed by (Van Rijn, 2007).

For the graded sediment, the transport rate is calculated for each size fraction separately as follows,

$$\frac{q}{\sqrt{(s-1)g d_{50}^3}} = \sum_{j=1}^{M} p_j \frac{q_j}{\sqrt{(s-1)g d_j^3}}, \tag{12}$$

where $q_j$is the net sediment transport rate for the fraction $j$with median diameter of $d_j$, $p_j$is the percentage of the fraction $j$, and $s$is the specific gravity of sediment. The transport rate $q_j$ of each fraction is calculated by a semi-unsteady half-cycle approach based on the effective nondimensional bottom shear stress ($\theta_{eff,j}$) or the Shields parameter obtained from modifying the bottom shear stress ($\theta_j$) by the hiding/exposure factor ($\varepsilon_{eff,j}$). The modification in the effective shear stress is such that the coarse fractions exposed in the bed surface layer receive a higher amount of shear stress and fine fractions experience a lower amount shear stress due to being armored by the coarse fractions (Van Rijn, 2007),

$$\theta_{eff,j} = \varepsilon_{eff,j} \theta_j, \tag{13}$$

and

$$\varepsilon_{eff,j} = \left( \frac{d_j}{d_{50}} \right)^{0.25}. \tag{14}$$

where $\theta_j$is the Shields parameter corresponding to the sediment bed of the uniform grain diameter $d_j$, and $\theta_{eff,j}$is the Shields parameter modified by $\varepsilon_{eff,j}$for the fraction $j$in the bed of graded sediment. $\varepsilon_{eff,j}$parameterizes the effects of exposure (of the coarse fraction) and armoring (of the fine fraction).

**Table 1**
List of coefficients used in k-ε model.

| $C_{1\varepsilon}$ | $C_{2\varepsilon}$ | $C_{3\varepsilon}$ | $C_{4\varepsilon}$ | $\sigma_k$ | $\sigma_\varepsilon$ | $\sigma_c$ |
|---|---|---|---|---|---|---|
| 1.44 | 1.92 | 1.2 | 0 | 1.0 | 1.3 | 1.0 |

## 3. Model domain setup and validation

In the present Reynolds-averaged formulation, the sheet flow was assumed to be fully developed in the streamwise (x) and spanwise (y) directions. Therefore, only one grid point was used in the two horizontal directions for the fluid phase, and periodic boundaries were used in x and y directions (i.e., one-dimensional-vertical, 1DV simulation). The bottom boundary was specified as a no-slip wall boundary while the top boundary was specified as a shear-free symmetric boundary. The model domain size was chosen to be $l_x = 20d_{50}$ in the streamwise direction, $l_y = 10d_{50}$ in the spanwise direction and 300 mm in the vertical (z) direction. The ratio of domain size to median grain diameter in the two horizontal directions was chosen following previous model studies (Calantoni and Thaxton, 2008; Maurin et al., 2015). To ensure the domain size in the two horizontal directions are sufficiently large for the particle phase, we also performed sensitivity analysis on the domain size for the well-sorted sand case as well as the moderately-sorted and poorly-sorted cases (see A4, BM cases in Table 2 and case P1 of Hassan and Ribberink (2005) to be discussed in Section 3.3) using $l_x = 30d_{50}$ and $l_y = 20d_{50}$. It was found that model results were not sensitive to the further increase of domain size and the resulting differences in net sediment transport rate were within 5%. Therefore, it was decided to use domain size with $l_x = 20d_{50}$ and $l_y = 10d_{50}$ for all simulations in order to maximize available computational resources. In the particle phase, the initial sediment bed thickness was set to be 12 mm, which was chosen such that a sufficient thickness of undisturbed bed (no less than 3 mm) was always present for different flow velocity intensities investigated in this study. In the fluid domain, uniform grid size of 1.25 mm was used in vertical direction for simulation of coarse sands ($d_{50}$ = 0.51 mm). Based on a sensitivity analysis on the grid size, finer grid sizes resulted in net sediment transport rates within 5% of difference. For model validations of

**Table 2**
Simulated particle size characteristics (see Fig. 7 for their cumulative size distributions).

| Distribution | $d_{90}/d_{10}$ | Category | $d_{10}$ (mm) | $d_{50}$ (mm) | $d_{90}$ (mm) |
|---|---|---|---|---|---|
| Uniform | 1 | uniform | 0.51 | 0.51 | 0.51 |
| A1 | 1.86 | very well-sorted | 0.36 | 0.51 | 0.67 |
| A2 | 2.56 | well-sorted | 0.32 | 0.51 | 0.82 |
| A3 | 3.41 | moderately-sorted | 0.27 | 0.51 | 0.92 |
| A4 | 4.16 | moderately-sorted | 0.25 | 0.51 | 1.04 |
| BM | 5.96 | poorly-sorted | 0.27 | 0.51 | 1.61 |

medium sand (case MA5010 of O'Donoghue and Wright (2004a) and case P1 of Hassan and Ribberink (2005)) the grids were refined to 0.35 mm in the bottom 50 mm of the fluid domain to ensure grid convergence. In the Lagrangian phase, the particles are tracked in meshless domain. To lower the number of particles used in each simulation and thus lower the computational cost, heavy particles of $2d_{50}$ diameter with a density 10 times greater than that of natural sand grains were specified at the first layer above the bottom boundary to generate an effectively immobile bottom-most layer (e.g., Calantoni and Thaxton, 2008). The initial sediment bed was prepared by gravitational settling of particles. To attain a similar initial bed composition for different grain size distributions, we intentionally prepared a well-mixed sediment bed for each run. To obtain an initially well-mixed sediment bed of graded sand, the gravitational settling began in a relatively high sediment concentration (volumetric sediment concentration about 0.5) to minimize the duration of settling and avoid the generation of normal grading (upward fining). For cases with wide size distribution, normal grading is unavoidable even with the methodology discussed above. Therefore, the initial bed of the non-uniform particle size distributions was formed by three pre-settled segments of 4 mm thickness generating 12 mm thick bed.

Model was extensively validated for the oscillatory sheet flow transport of well-sorted and graded sands. First, using the laboratory data of O'Donoghue and Wright (2004a, 2004b) an extensive model validation was performed for the well-sorted medium sand ($d_{50}$ = 0.28 mm) and coarse sand ($d_{50}$ = 0.51 mm) driven by velocity-skewed oscillatory flow (Section 3.1). Next, using the laboratory data of Van der A et al. (2010) the model was further evaluated for predicting the net sediment transport rates of the well-sorted coarse sand ($d_{50}$ = 0.46 mm) under acceleration-skewed oscillatory flows (Section 3.2). Furthermore, the model validation was extended to the graded sand with bimodal size distribution (mixture of $d_{50}$ = 0.21 mm and $d_{50}$ = 0.97 mm, Section 3.3) using the laboratory data of Hassan and Ribberink (2005), and the predicted fractional and total net transport rates were compared with the measured data.

### 3.1. Well-sorted sand under velocity-skewed flow

Using laboratory data of O'Donoghue and Wright (2004a, 2004b) the model validation was performed for sheet flow in a water tunnel driven by an onshore (positive) velocity-skewed oscillatory flow (flow A5010) with well-sorted medium sand of median grain diameters, $d_{50}$ = 0.28 mm ($d_{10}$ = 0.17 mm, $d_{90}$ = 0.45 mm, $d_{90}/d_{10}$ = 2.64), and very-well sorted coarse sand of $d_{50}$ = 0.51 mm (see A1 distribution in Table 2). The oscillatory flow in the tunnel corresponded to a second-order Stokes wave motion with velocity amplitude of 1.5 m/s in crest period (Fig. 1 (a)).

To make a fair comparison between model results and measured data, we shifted the vertical elevation such that the modeled and measured concentration profiles at the flow reversal (t = 0) intersect at concentration of 0.55. Once this shift was determined in each case, it was used consistently for all the comparisons of the case. For the medium sand case ($d_{50}$ = 0.28 mm), reasonably good agreements between the modeled and measured sediment concentration profiles at the instants of flow reversals (Fig. 1 (b) and (d)), peak flow during crest (Fig. 1 (c)), and peak flow during trough (Fig. 1 (e)) were observed. Here, we

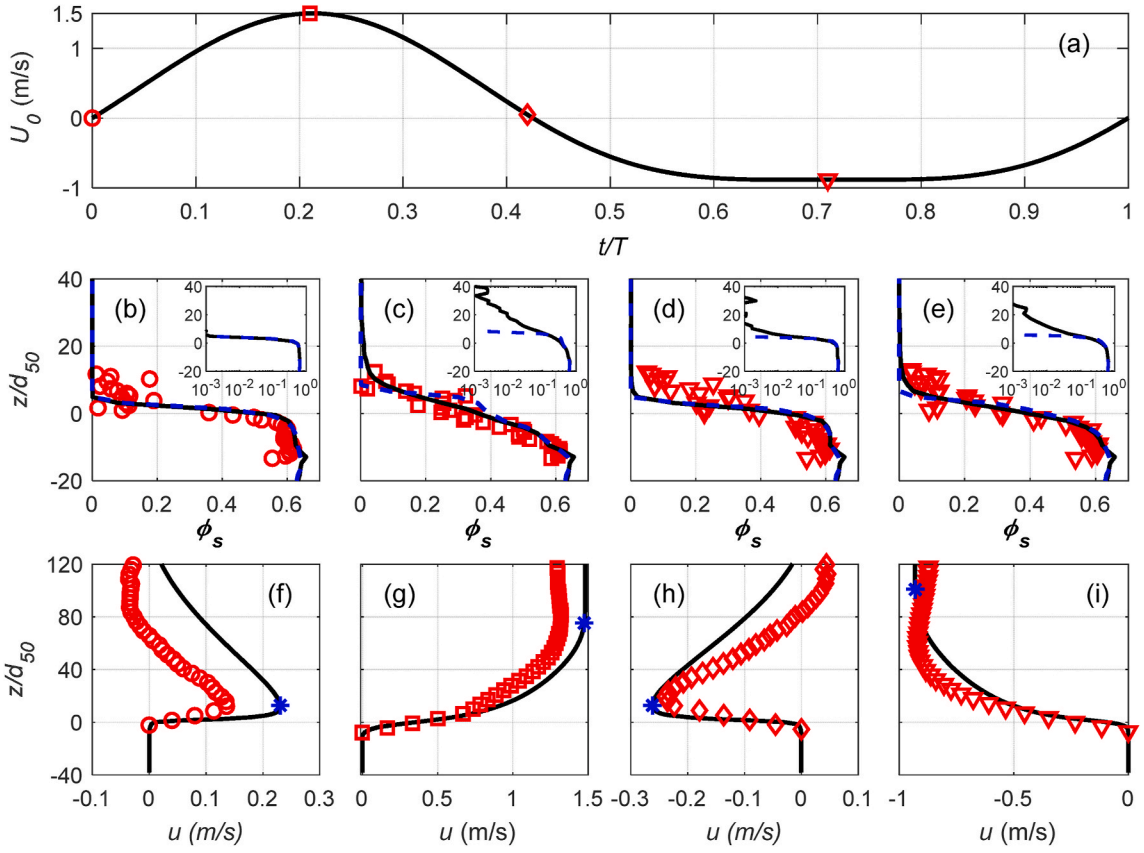


**Fig. 1.** (a) Time series of free-stream velocity for case MA5010 ($d_{50}$ = 0.28 mm) of O'Donoghue and Wright (2004a, 2004b) used to drive the model. Modeled sediment concentration profiles using the complete model (solid black) and the ones with eddy interaction model switched off (dashed blue) are compared with measured data (symbols) at (b) the off-onshore flow reversal ($t/T$ = 0); (c) the peak flow during crest ($t/T$ = 0.21); (d) the on-offshore flow reversal ($t/T$ = 0.42); (e) the peak flow during trough ($t/T$ = 0.71). Panels (f), (g), (h) and (i) show the corresponding modeled (line) and measured (symbols) fluid velocity profiles. To identify the instantaneous boundary layer thickness, the modeled velocity overshoot location is signified with a star symbol. (For interpretation of the references to color in this figure legend, the reader is referred to the Web version of this article.)

also performed another simulation with the eddy-interaction model switched off to illustrate its capability to model turbulent suspension (dashed blue lines in the inset of Fig. 1 (b)–(e)). At the peak flow instants (Fig. 1 (c) and (e)), the simulation without the eddy-interaction model cannot predict suspended load transport above the sheet flow layer with concentration small than about 0.1. Comparison of velocity profiles at the flow reversals (Fig. 1 (f) and (h)) and the peak flow during crest (Fig. 1 (g)) showed that the velocity structure, particularly the overshoot velocity location, was predicted well by the model (see blue stars in each panel) with a small difference of about 5%. At the peak flow during trough (Fig. 1 (i)), however, the model over-predicted the elevation of the overshoot velocity. This discrepancy may be due to a common deficiency of two-equation turbulence closure in oscillatory sheet flows (Amoudry, 2014; Cheng et al., 2017). There were also a few uncertainties in the model-data comparison. The measured velocity profiles used here correspond to averaged velocity profile obtained from the three mixed sand cases with $d_{50}$ ranging from 0.19 to 0.28 mm. According to O'Donoghue and Wright (2004a, 2004b), this was the only available velocity data in their experiments. Secondly, there is a return flow present in the tunnel experiment which introduced an offset of velocity far from the bed and this returning flow was not modeled here. For instance, at the peak flow during crest, the free stream velocity was supposed to reach 1.5 m/s according to the prescribed forcing while the measured data only reached about 1.35 m/s (see Fig. 1 (g)).

We next carried out model validation for the coarse sand case CA5010 ($d_{50} = 0.51$ mm, see A1 in Table 2) of O'Donoghue and Wright (2004a, 2004b). A good agreement was obtained in concentration profiles and it was not presented here for brevity. Instead, we focused on the model-data comparison of time-dependent erosion depth, sheet flow sediment transport rate, and sediment flux profiles in the sheet flow layer. Fig. 2 (b) shows the modeled and measured time series of erosion depth, which was defined as the depth from the initially undisturbed bed surface to the instantaneous immobile bed level. Due to scattering of measured data, O'Donoghue and Wright (2004a, 2004b) developed a method to identify the inflection point of a concentration profile and fitted the profile with a curve to obtain the instantaneous immobile bed location. This method typically gave a concentration at the immobile bed around 0.55~0.6. Therefore, the volumetric concentrations of 0.55 and 0.6 were both examined to identify the instantaneous immobile bed level calculated by the model. It can be seen that model was able to capture the peak erosion depth at both crest and trough periods using the non-erodible bed concentration of 0.55, although the model results showed a slight phase difference during flow reversal. Based on the model results, the sediment velocity can be as large as 2 cm/s at peak flow during crest at the location where the sediment concentration was 0.55. Using a sediment concentration of 0.6, the peak sediment velocity dropped considerably to about 0.12 cm/s. As can be seen in Fig. 2 (b), using sediment concentration of 0.6 resulted in 25%–35% larger erosion depth at the instants of peak flow during crest and trough periods. The creeping particle motions can still occur at high sediment concentration of 0.55–0.6, which caused uncertainties in identifying erosion depth. However, the corresponding particle velocity was on the order of mm/s and these uncertainties contributed only a minor amount of the total sediment transport rate during sheet flow.

The sheet flow layer was defined by O'Donoghue and Wright (2004a) as the layer from the instantaneous non-erodible bed level to the level where sediment concentration is 0.08. Time series of the sediment transport rate in the sheet flow layer calculated by the model showed a good agreement with the measured data, although the model slightly under-predicted the transport rate near the peak flows (Fig. 2 (c)). Nevertheless, the overall agreement for wave-period-averaged total sediment transport rate was good. Comparison of sediment flux profiles at peak flow instants during crest (Fig. 2 (e)) and during trough (Fig. 2 (g)) as well as instants during onshore and offshore acceleration (Fig. 2 (d), (f)) also shows a good agreement between the modeled sediment fluxes and the values obtained from measurements (as a product of measured concentration and velocity profiles). As a result of onshore (positive) velocity skewness, the wave-period-averaged total sediment transport rate (net transport rate) predicted by the model was 48 mm$^2$/s, where the measured value was 44 mm$^2$/s. The numerical simulations were performed for 20 wave periods, and the net sediment transport rates were obtained by time-averaging over the last 10 wave periods when sediment transport already reached quasi-steady state evaluated in terms of establishing an equilibrium wave-shape streaming (e.g., Kranenburg et al. (2012)).

Fig. 3 shows snapshots of particles in the computational domain, where the color of each particle represents its diameter relative to $d_{50}$. The particles were initially well-mixed in the bed (Fig. 3 (a)). After the action of 10 waves, the formation of inverse grading (upward coarsening), namely the coarser particles covered the surface layer of the sediment bed and finer particles were shielded by the exposed coarser particles, can be clearly seen (Fig. 3 (b)). Subsequently, at the peak flow

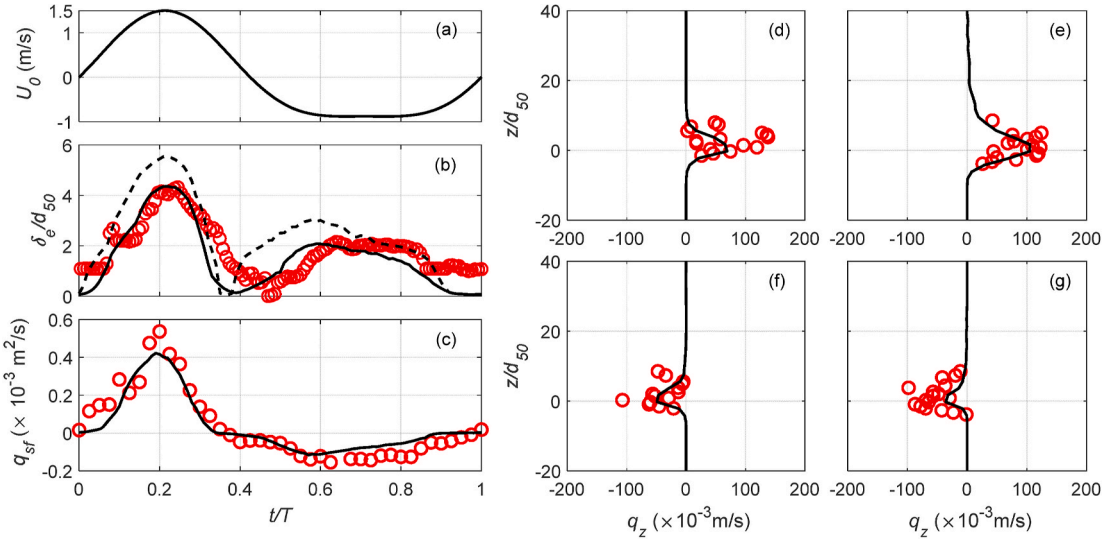


**Fig. 2.** (a) Time series of free stream velocity for case CA5010 ($d_{50} = 0.51$ mm) of O'Donoghue and Wright (2004a, 2004b). (b) Measured (symbols) and modeled time series of the erosion depth based on the non-erodible bed concentration of 0.55 (solid) and 0.6 (dashed). (c) Time series of sediment transport rate in sheet flow layer. Measured (symbols) and modeled (line) sediment flux profiles in sheet flow layer for case CA5010 at (d) the onshore acceleration during crest ($t/T = 0.11$), (e) the peak flow during crest ($t/T = 0.21$), (f) offshore acceleration during trough ($t/T = 0.57$), (g) the peak flow during trough ($t/T = 0.71$).

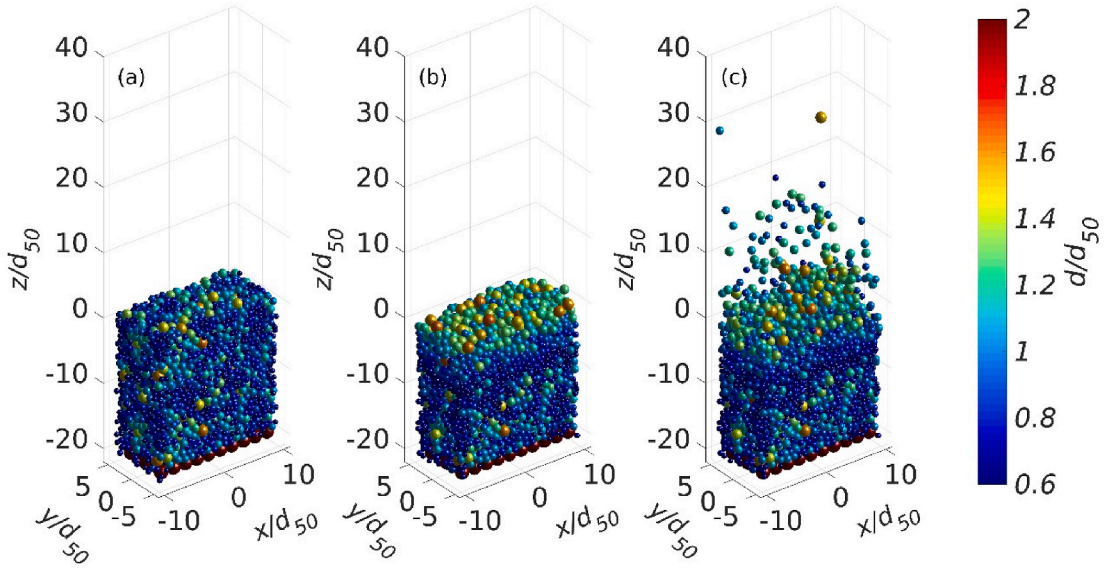


**Fig. 3.** Snapshots of sediment particles in the model domain corresponding to the case CA5010 ($d_{50}$ = 0.51 mm) of O'Donoghue and Wright (2004a, 2004b); (a) initial bed; snapshots at (b) flow reversal ($t/T$ = 0) and (c) peak flow during crest ($t/T$ = 0.21) of the 10th flow cycle.

crest (Fig. 3 (c)) when a significant amount of sediment particles was mobilized and suspended, we observed that a majority of them were associated with the coarse fraction (light blue, green and yellow) while the fine fraction (dark blue) was mainly armored in the lower layer. Interestingly, although this was a case of very well-sorted sand ($d_{90}/d_{10}$ = 1.86, see Table 2), the inverse grading was already clear. Comparing the initial sediment bed and the bed affected by waves (Fig. 3 (a) and (b)), the deeper portion of the sediment bed was unchanged ($z/d_{50} \lesssim$-8) which can be referred to as undisturbed bed. On the other hand, the upper portion of the sediment bed ($z/d_{50} \gtrsim$-8) was affected by vertical sorting, which was referred to as the active layer (Hassan and Ribberink, 2005). Motivated by this result, Section 3.3 will focus on model validation for mixed sand while Section 4 will focus on the effect of vertical sorting on wave-driven sheet flow sediment transport.

### 3.2. Well-sorted sand under acceleration-skewed flows

Using water tunnel data of Van der A et al. (2010) we validated the model for sheet flow driven by onshore acceleration-skewed oscillatory flows for well-sorted coarse sand ($d_{50}$ = 0.46 mm, $d_{10}$ = 0.35 mm, $d_{90}$ = 0.58 mm). The acceleration-skewed oscillatory flows were generated in this experiment with different values of acceleration skewness $\beta$ (see its definition in Section 4.1). We simulated cases S556015c, S606015c, S656015c, and S706015c reported by Van der A et al. (2010) all having the same oscillatory period of 6 s and velocity amplitude of 1.3 m/s but with different acceleration skewness $\beta$ values of 0.58, 0.62, 0.66, and 0.71, respectively. Model predictions of the wave-period-averaged net sediment transport rates are compared with the measured values in Fig. 4 (a). The model is able to predict the net sediment transport rates driven by acceleration-skewed oscillatory flows where all the predicted values are well within a factor two of measured data. The model tends to under-predict onshore transport for high acceleration skewness cases

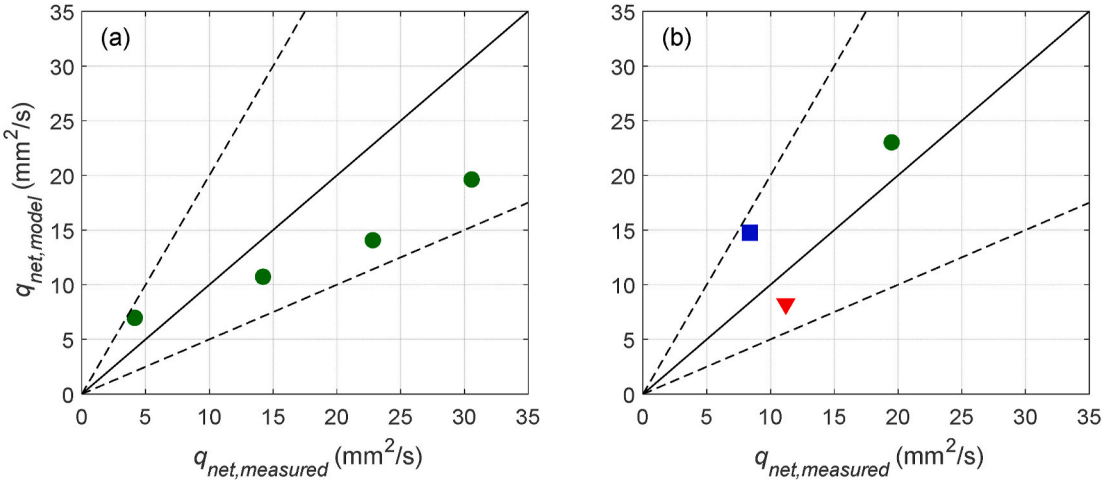


**Fig. 4.** (a) Agreement of wave-period-averaged transport rates of well-sorted coarse sand ($d_{50}$ = 0.51 mm) driven by acceleration-skewed oscillatory flows between measured data reported by Van der A et al. (2010) and modeled results. (b) Model predictions of fractional and total net transport rate compared to measured data corresponding to the case P1 of Hassan and Ribberink (2005) with bimodal size distribution. The blue square represents the coarse fraction ($d_{50}$ = 0.97 mm, 30% of the mixture), the red triangle represents the fine fraction ($d_{50}$ = 0.21 mm, 70% of the mixture), and the green circle corresponds to the net transport rate of the total mixture. (For interpretation of the references to color in this figure legend, the reader is referred to the Web version of this article.)

probably due to the limitation of the present 1DV model domain which cannot capture shear instabilities of the sheet flow layer during momentary bed failure (Foster et al., 2006; Kim et al., 2019).

### 3.3. Mixed sand under velocity-skewed flow

Hassan and Ribberink (2005) performed extensive measurements of mixed (bimodal) sand transport driven by oscillatory flows. To evaluate the capability of the model to simulate the mixed sand transport, we selected a sediment mixture with median grain diameter $d_{50} = 0.24$ mm resulted from 30% of coarse fraction with $d_{50} = 0.97$ mm and 70% of fine fraction with $d_{50} = 0.21$ mm. The resulting median grain diameter for the entire mixture was $d_{50} = 0.24$ mm. We simulated the case P1 which corresponded to the onshore velocity-skewed flow with the peak flow velocity of 1.08 m/s that yields a Shields parameter ($\theta \approx 1.3$) similar to the coarse sand case tested in Sections 3.1 and 3.2. Fig. 4 (b) shows the comparison of the model predictions of the fractional and total net transport rates with the measured data. The model slightly under-predicted the net transport rate of the fine fraction. The model also over-predicted net transport rate of the coarse fraction but the agreement is within a factor two of the measured value. The net transport rate of the total mixture was over-predicted by about 20%. The agreement between model results and measured data was acceptable to allow us to further use the model to investigate vertical sorting even in bimodal distribution.

The snapshot of particles in the simulation domain corresponding to the case P1 of Hassan and Ribberink (2005) are shown in Fig. 5. Particles are initially well-mixed in the sediment bed with fine particles accumulated near the bed surface due to initial gravitational settling (see Fig. 5 (a)). After the action of 10 flow cycles, formation of inverse vertical sorting can clearly be observed in the bed surface layer (Fig. 5 (b)), where the coarse particles migrated to the bed surface and fine particles were armored below the coarse particles. The percentage of coarse fraction in the bed is illustrated for the initial bed (Fig. 5 (c), dashed line) and the bed after 10 flow cycles (Fig. 5 (c), solid line). Near the surface ($-5d_{50} < z < 0$) the initial bed was dominated by the fine fraction with the percentage of coarse fraction approaching to zero at the upper most layer. The trend was reversed after 10 flow cycles where the coarse fraction dominated in the surface layer contributing to more than 75% of the mixture. Just below the surface layer (see solid line in Fig. 5 (c) between $-10 < z/d_{50} < -4$), the composition is dominated by the fine fraction where the coarse fraction contributed less than 10%. The vertical sorting structure reported here is qualitatively similar to the laboratory observation (see Fig. 22 of Hassan and Ribberink (2005)). In Section 4.2, a more in-depth analysis on vertical sorting and their effect on sediment transport will be presented.

## 4. Results

### 4.1. Design of simulations

Thirty-eight sets of numerical simulations were performed to investigate the effect of sediment size gradation on sediment transport driven by oscillatory flows. The numerical simulations were organized as follows. First, transport of the graded particles was investigated for six different grain size distributions (Table 2) under onshore velocity-skewed oscillatory flows to explore the effect of armoring and exposure for different size distributions (Section 4.2). Since erosion depth and active layer thickness depend on flow velocity intensity (Hassan and Ribberink, 2005), we hypothesized that gradation effects must also depend on flow velocity intensity. Therefore, two velocity-skewed flows with low and high values of root-mean-square velocity and velocity skewness were compared for six different size distributions shown in Table 2. Then, the results of the graded and uniform-sized particles were contrasted under various oscillatory flow shapes and velocity intensities to investigate the grading effect on sediment transport rate (Section 4.3~4.5).

The sediment size characteristics and flow conditions were summarized in Tables 2 and 3, respectively. The $u_{max}$, $u_{min}$ and $u_{rms}$ are the maximum, minimum and root mean square velocities, respectively. $u^3$ is the wave-averaged third-moment of velocity which the net sediment transport rate driven by velocity-skewed oscillatory flows can be quantified upon (Ribberink and Al-Salem, 1994). The R and β are parameters to represent the velocity and acceleration skewness, respectively. These parameters are defined as follows,

$$R = \frac{u_{max}}{u_{max} - u_{min}}, \tag{15}$$

and

$$\beta = \frac{a_{max}}{a_{max} - a_{min}}. \tag{16}$$

In the literature, the wave shape is more commonly quantified by the skewness ($S_k$) and asymmetry ($A_s$) of the near bed velocity calculated as (Elgar et al., 1988),

$$S_k = \frac{\langle u^3 \rangle}{\langle u^2 \rangle^{3/2}}, \tag{17}$$

and

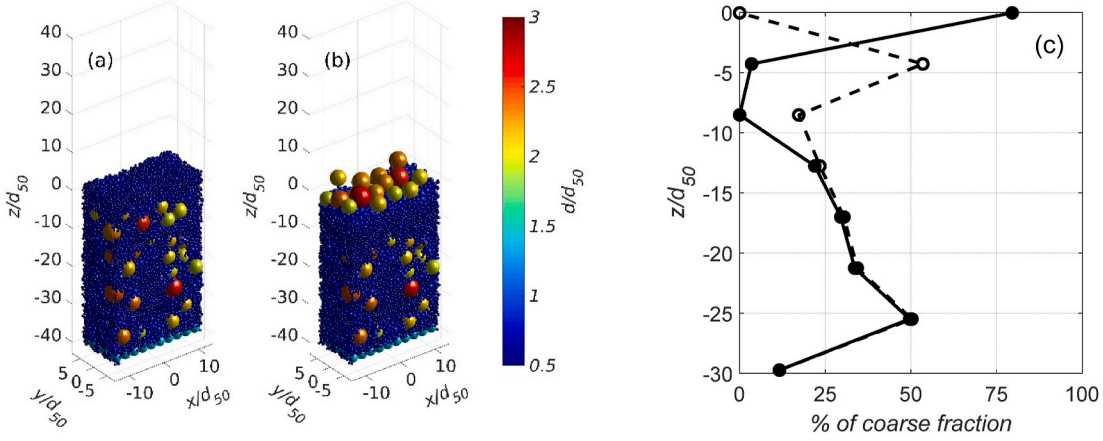


**Fig. 5.** Snapshots of sediment particles in the simulation domain of the bimodal size distribution corresponding to the case P1 of by Hassan and Ribberink (2005); (a) initial bed, and (b) flow reversal ($t/T = 0$) of the 10th flow cycle. (c) Percentage of coarse fraction in the sediment bed corresponding to the initial bed (dashed line) and the bed after 10 flow cycles (solid line).

**Table 3**
Simulated oscillatory flow conditions.

| Flow ID | T (s) | $u_{max}$ (m/s) | $u_{min}$ (m/s) | $u_{rms}$ (m/s) | $R$ | $\beta$ | $S_k$ | $A_s$ | $<u^3>$ (m$^3$/s$^3$) |
|---|---|---|---|---|---|---|---|---|---|
| I88R63B50 | 5 | 1.50 | −0.90 | 0.88 | 0.63 | 0.50 | 0.48 | 0 | 0.32 |
| I88R70B50 | 5 | 1.90 | −0.81 | 0.88 | 0.70 | 0.50 | 0.92 | 0 | 0.63 |
| I88R78B50 | 5 | 2.34 | −0.66 | 0.88 | 0.78 | 0.50 | 1.43 | 0 | 0.98 |
| I109R63B50 | 5 | 1.87 | −1.12 | 1.09 | 0.78 | 0.50 | 0.48 | 0 | 0.63 |
| I109R70B50 | 5 | 2.35 | −1.01 | 1.09 | 0.70 | 0.50 | 0.92 | 0 | 1.20 |
| I109R78B50 | 5 | 2.90 | −0.82 | 1.09 | 0.78 | 0.50 | 1.43 | 0 | 1.86 |
| I92R50B62 | 6 | 1.30 | −1.30 | 0.92 | 0.50 | 0.62 | 0 | −0.25 | 0 |
| I92R50B71 | 6 | 1.31 | −1.31 | 0.92 | 0.50 | 0.71 | 0 | −0.46 | 0 |
| I92R50B78 | 6 | 1.32 | −1.32 | 0.92 | 0.50 | 0.78 | 0 | −0.64 | 0 |
| I109R50B62 | 6 | 1.54 | −1.54 | 1.09 | 0.50 | 0.62 | 0 | −0.25 | 0 |
| I109R50B71 | 6 | 1.55 | −1.55 | 1.09 | 0.50 | 0.71 | 0 | −0.46 | 0 |
| I109R50B78 | 6 | 1.56 | −1.56 | 1.09 | 0.50 | 0.78 | 0 | −0.64 | 0 |
| I88R57B57 | 5 | 1.45 | −1.09 | 0.88 | 0.57 | 0.57 | 0.30 | −0.16 | 0.21 |
| I88R60B54 | 5 | 1.53 | −1.02 | 0.88 | 0.60 | 0.54 | 0.44 | −0.10 | 0.30 |
| I88R54B60 | 5 | 1.36 | −1.15 | 0.88 | 0.54 | 0.60 | 0.17 | −0.22 | 0.12 |

$$A_s = \frac{\langle H(u)^3 \rangle}{\langle H(u)^2 \rangle^{3/2}}, \tag{18}$$

where $H(u)$is the Hilbert transform of the velocity time series, and the angle brackets denote the time averaging. The pure onshore velocity-skewed waves have positive $S_k$ with zero $A_s$, while the pure onshore acceleration-skewed waves have zero $S_k$ with negative $A_s$. The values of $S_k$ and $A_s$ corresponding to the simulated flow conditions are also reported in Table 3.

To generate time-series of near-bed orbital velocity with prescribed values of velocity and acceleration skewness to drive the numerical simulations, the analytical formula proposed by Abreu et al. (2010) was used,

$$u(t) = U_w f \frac{\left[sin(\omega t) + \frac{rsin\varphi}{1+\sqrt{1-r^2}}\right]}{[1 - rcos(\omega t + \varphi)]}, \tag{19}$$

where $U_w$is the amplitude of the wave orbital velocity, $r$is an index of

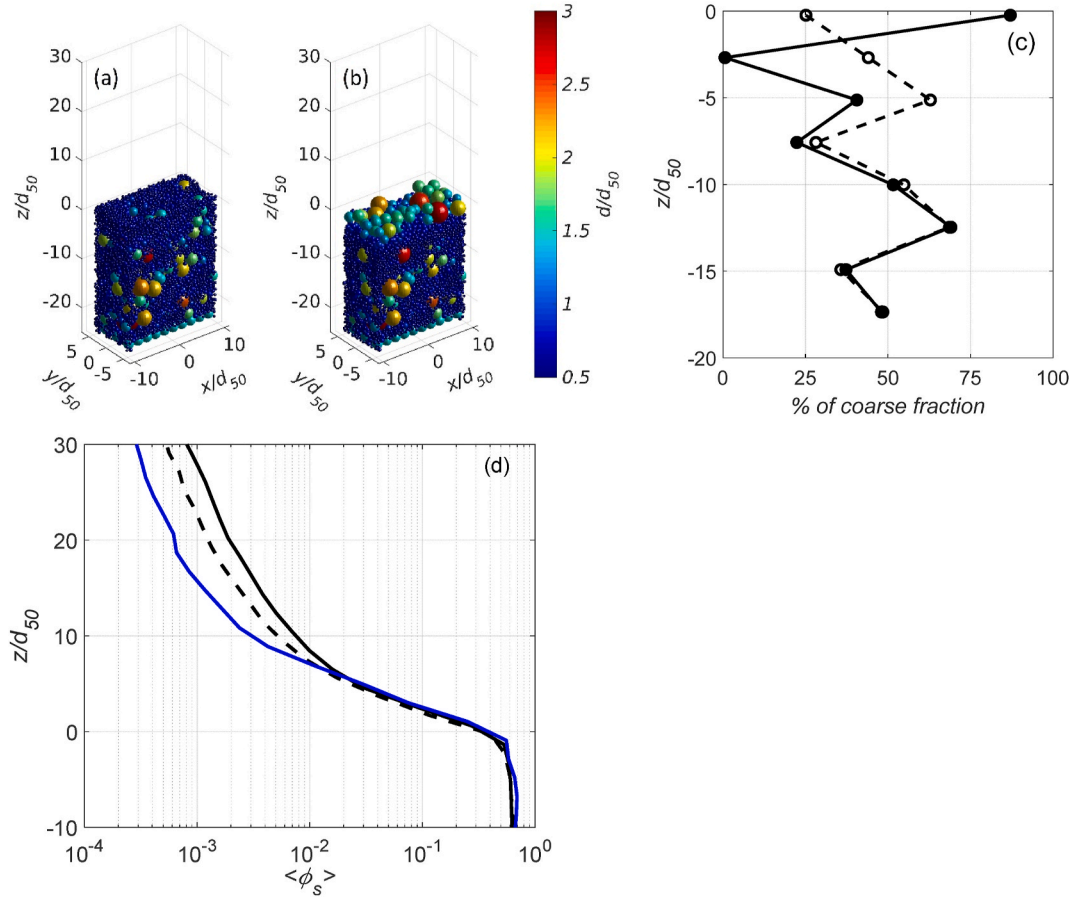


**Fig. 6.** Snapshots of sediment particles in the simulation domain of the bimodal size distribution (BM) under velocity-skewed flow condition A5010 of O'Donoghue and Wright (2004a, 2004b); (a) initial bed, and (b) flow reversal ($t/T = 0$) of the 10th flow cycle. (c) Percentage of coarse fraction of the sediment bed corresponding to the initial bed (dashed line) and the bed after 10 flow cycles (solid line). (d) Wave-period-averaged sediment concentration profiles under flow A5010 of O'Donoghue and Wright (2004a, 2004b) of uniform-sized particles (solid back line), A1 (very well-sorted, dashed black line), and BM (poorly-sorted, solid blue line) distributions. (For interpretation of the references to color in this figure legend, the reader is referred to the Web version of this article.)

nonlinearity ($r = 0$ corresponds to linear wave orbital velocity), $f$is a function of $r$($f = \sqrt{1-r^2}$), $\omega$is the frequency. Importantly, $\varphi$is a waveform parameter varying from -90° to 0°, where $\varphi$closer to -90° (0°) yields higher velocity skewness (acceleration skewness).

### 4.2. Effect of sediment size distribution

Motivated by the modal-data comparison with Hassan and Ribberink (2005) (see Section 3.3) for bimodal sand transport under velocity-skewed flows, we first present a simulation of bimodal size distribution (BM in Table 2) having the same $d_{50}$ and under the same wave forcing corresponding to the coarse sand case CA5010 of O'Donoghue and Wright (2004a). To achieve the same $d_{50}$ of 0.51 mm and to generate a very wide (poorly-sorted) size distribution ($d_{90}/d_{10} = 5.96$, see BM in Table 2), the bimodal distribution consisted of 55% of median diameter of $d_{50} = 0.35$ mm (fine fraction; $d_{10} = 0.25$ mm, $d_{90} = 0.5$ mm) and 45% of median diameter of $d_{50} = 1.3$ mm (coarse fraction; $d_{10} = 0.92$ mm, $d_{90} = 1.87$ mm). It is worth mentioning that the choice of fine and coarse fractions and the corresponding median grain diameters to generate a bimodal distribution is not unique and we selected the fine fraction sediment size in the range of medium sand to be consistent with the model validation (Section 3).

Similar to the earlier bimodal case presented in Section 3.3, the initial sediment bed showed a slight normal grading (fining upward) profile in the surface layer (-5<$z/d_{50}$ < 0, see Fig. 6 (a) and dashed line in Fig. 6 (c)) because of the initial gravitational settling. However, after 10 flow cycles, inverse grading was again evident (see Fig. 6 (b) and solid line in Fig. 6 (c)), where the coarse fraction contributed to more than 75% of the mixture within the surface layer ($z/d_{50} > -2$), while in the lower levels (-8 < $z/d_{50}$ < -2), sediments were mostly of fine fraction. Deeper into the bed (-15 < $z/d_{50}$ < -8), the difference between the initial and final profiles was very small, suggesting that only creeping motion of particles had occurred. It is noted that the maximum erosion depth corresponded to $z/d_{50} = -3.5$ (based on non-erodible sediment concentration of 0.6) which was notably smaller than the active layer depth ($z/d_{50} \approx -8$) for very wide grain size distribution (BM). The difference may be attributed to the dominance of relatively large particles in the bed surface layer (Fig. 6 (b), light blue, yellow and red), which may avoid deeper erosion and horizontal movement under the oscillatory flow motion. However, vertical relative migration between finer particles and coarser particles were still possible (Rosato et al., 1987). This can also be confirmed by looking at the maximum erosion depth of well-sorted A1 distribution (Fig. 2 (b), dashed line), being about 50% larger than that of the BM distribution under the same flow condition. Significant vertical sorting in BM distribution clearly showed pronounced armoring effect by reducing erosion depth.

To see the effect of vertical sorting on hindering sediment suspension (Wiberg et al., 1994), the wave-period-averaged concentration profiles of A1 and BM distributions under the same oscillatory flow condition (flow A5010 of O'Donoghue and Wright (2004a))) are compared in Fig. 6 (d) along with the profile corresponding to the uniform-sized particles with the same median grain diameter ("Uniform" in Table 2). The comparison confirmed that armoring of suspended load was more pronounced for the BM size distribution as the decay of concentration in suspension layer ($z/d_{50} > 6$) was more drastic compared with A1 and Uniform distributions. Furthermore, we observed that even for narrow size distribution (A1), the armoring was effective as the suspended sediment concentration was notably smaller than that of uniform-sized particles (compare dashed line with solid black line in Fig. 6 (d)). In short, the armoring effect of suspended load predicted by the present model was qualitatively similar to the field observation reported by Wiberg et al. (1994) and it can be expected that exposure of coarse grains and armoring of fine grains play a role in the total sediment transport rate.

To further quantify how sediment with different size distributions responds to the velocity-skewed oscillatory flow forcing, three additional sediment size distributions were tested (see Table 2). Based on the classification proposed by Folk and Ward (1957), the six sediment size distributions investigated here included very well-sorted, moderately-sorted and poorly-sorted particles. Fig. 7 shows the cumulative grain size distribution for simulated sand types plotted in the horizontal axis as the total weight percentage that is finer than a particular diameter, where the two modes of bimodal size distribution (BM; blue) can be compared to the single mode of unimodal size distributions (A1, A2, A3, A4; black). The width of the grain size distribution can also be quantified by the ratio of $d_{90}/d_{10}$ (see Table 2).

We first present the vertical grading features in the sediment bed in order to establish the importance of armoring and exposure in the resulting sediment transport. Fig. 8 shows the vertical profiles of median grain diameter for four different particle size distributions (A1, A2, A3, and A4) in the initial bed (Fig. 8 (a)), the bed after 10 flow cycles driven by low (I88R63B50, Fig. 8 (b)) and high (I109R78B50, Fig. 8 (c)) velocity intensity and skewness. It was evident that under both flow intensities, vertical sorting of sediment grains evolved into inverse grading, even though the initial bed was well-mixed. Moreover, as the grain size distribution became wider, there was a more pronounced inverse grading signified by wider grain size variation. The sorting process extended to as deep as -15 < $z/d_{50}$ < -12 under high velocity intensity (Fig. 8 (c)), while under low velocity intensity, the sorting extended to $z/d_{50} \approx -8$ (Fig. 8 (b)). To relate vertical sorting with horizontal transport, it is important to also discuss their erosion depths. The deepest erosion based on the non-erodible bed concentration of 0.6 for the high velocity intensity condition reached to as deep as -15 < $z/d_{50}$ < -12, while for the low velocity intensity condition, the erosion reached to -4.5 < $z/d_{50}$ < -5.5. Although the erosion depth is slightly smaller than active layer depth for lower velocity intensity, the erosion depths for both flow conditions are sufficiently deep to cover the surface layer where coarse fraction is dominant. Therefore, we expect the sediment transport processes are dictated by: 1) the coarse fraction armors the surface layer while being transported in the sheet flow layer; 2) the amount of fine fraction in suspension is limited by the mobility of coarse fraction.

Fig. 9 shows the wave-period-averaged (net) transport rates for all grain size distributions, plotted according to their $d_{90}/d_{10}$ value, driven by low and high flow velocity intensity and skewness. Notice that the cases with uniform grain size are shown with $d_{90}/d_{10} = 1$. In general, gradation effect ($d_{90}/d_{10} > 1$) led to the enhanced net onshore (positive) transport rates driven by onshore velocity-skewed flows in both flow conditions, and the rate of increase can be up to 20–30%. Considering the inverse grading features observed in Fig. 8, there are several possibilities that gradation effects can increase net onshore transport rate for onshore velocity-skewed flow. The net transport rate driven by the present onshore velocity-skewed flows is a summation of the positive transport during crest flow and the negative transport during trough flow. Hence, increased onshore transport rate may be due to reduction of transport during trough period. Since the surface layer is armored by coarse particles (see Fig. 8), this reduction can be caused by the coarser fraction now having lower mobility (relative to more well-sorted distributions under the same forcing) while the suspended fine fraction is limited by armoring. On the other hand, the increased onshore transport rate can also be directly caused by the enhancement of transport in the coarse fraction during crest period for more energetic flow condition. In a given control volume containing water and sediment, the total sediment volume is slightly larger when having some coarse particles filled with fine particles in the pore as compared to that of uniform-sized counterpart. Therefore, when flow intensity is sufficiently large to even mobilize the coarsest fraction, the total transport may be slightly enhanced.

Moreover, we noticed that the increasing trend in net sediment transport rate in unimodal conditions (uniform and A1~A4 in Table 2) peaked at $d_{90}/d_{10} = 3.41$ due to larger degree of sorting (Fig. 9). There

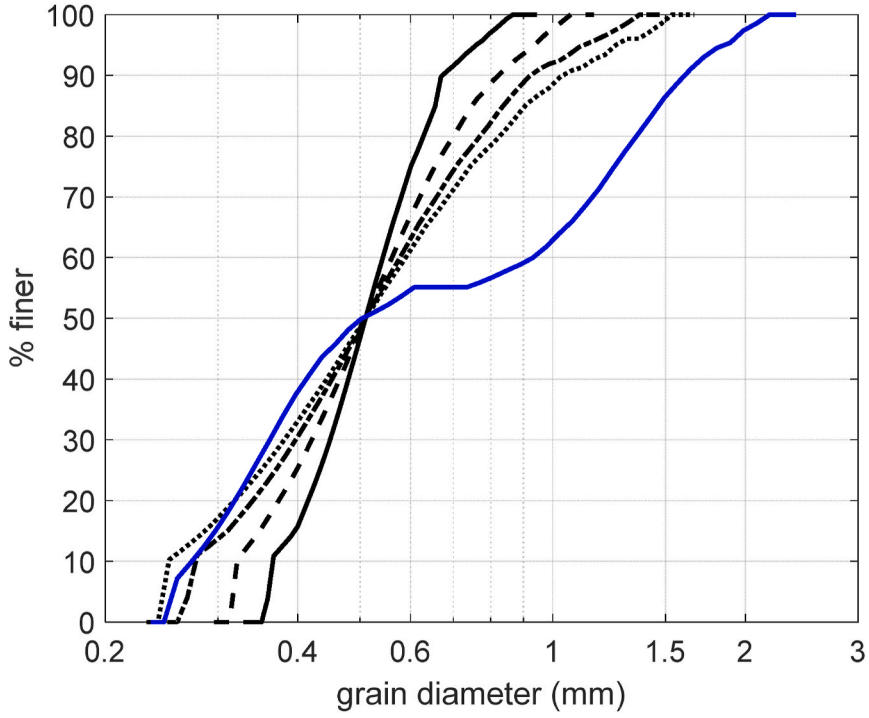


**Fig. 7.** Cumulative size distribution of A1 (solid black, very well-sorted), A2 (dashed black, well-sorted), A3 (dash-dot black, moderately-sorted), A4 (dotted black, moderately-sorted) and BM (solid blue, poorly-sorted) shown in Table 2. (For interpretation of the references to color in this figure legend, the reader is referred to the Web version of this article.)

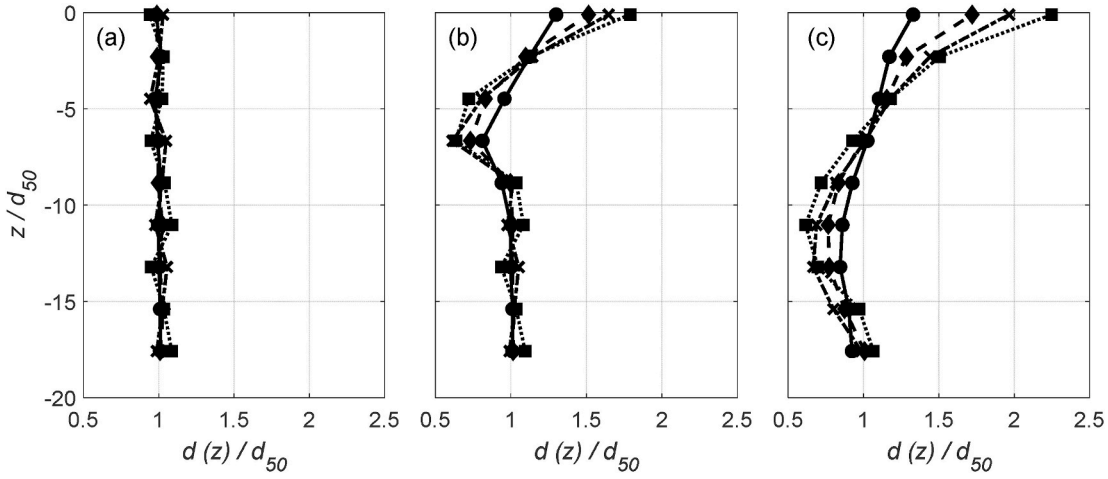


**Fig. 8.** Vertical distribution of median grain diameter normalized by $d_{50}$ (= 0.51 mm) in the sediment bed for (a) the initial bed, and results for after 10 flow cycles for (b) low velocity intensity condition I88R63B50, and (c) high velocity intensity condition I109R78B50. Results are presented for particle size distributions A1 (circles), A2 (diamonds), A3 (crosses), and A4 (squares).

seems to be a critical degree of sorting such that further increase of sorting can no longer enhance net positive transport for positive velocity-skewed flows. Similar features have been reported by another Eulerian-Lagrangian model study by Calantoni and Thaxton (2008). They argued that for very wide size distributions, the dimensional grain size may also be important in addition to size ratio (e.g., $d_{90}/d_{10}$). Motivated by these observations, we quantified the mobilization of the coarse and fine fractions by calculating the net transport rates corresponding to the coarse particles (larger than the median diameter, $d_{50}$) and those of the fine particles (finer than $d_{50}$) of the five graded size distributions under velocity-skewed flows of low (I88R63B50) and high (I109R78B50) velocity intensities (Fig. 10 (a) and (b), see Table 4). It is clear that net transport rates associated with the coarse fraction are significantly larger than those of fine fraction for both high and low velocity intensities (compare red symbols with black symbols in Fig. 10 (a) and (b)). The variabilities of net (total) transport rate with respect to $d_{90}/d_{10}$ shown in Fig. 9 mainly followed that of coarse fractions shown in Fig. 10 (a) and (b). The net transport rates associated with fine fraction for low velocity intensity scenario were almost identical for A1, A2, A3 and A4 (see black circles in Fig. 10(b)) because they had similar active layer thickness (see Fig. 8) and erosion depth. For high velocity intensity condition, the net transport rates due to fine fraction show a more pronounced decreasing trend from very well-sorted to moderately-sorted distribution due to larger change in active layer thickness and erosion depth.

The importance of coarse fraction is more evident by looking into the

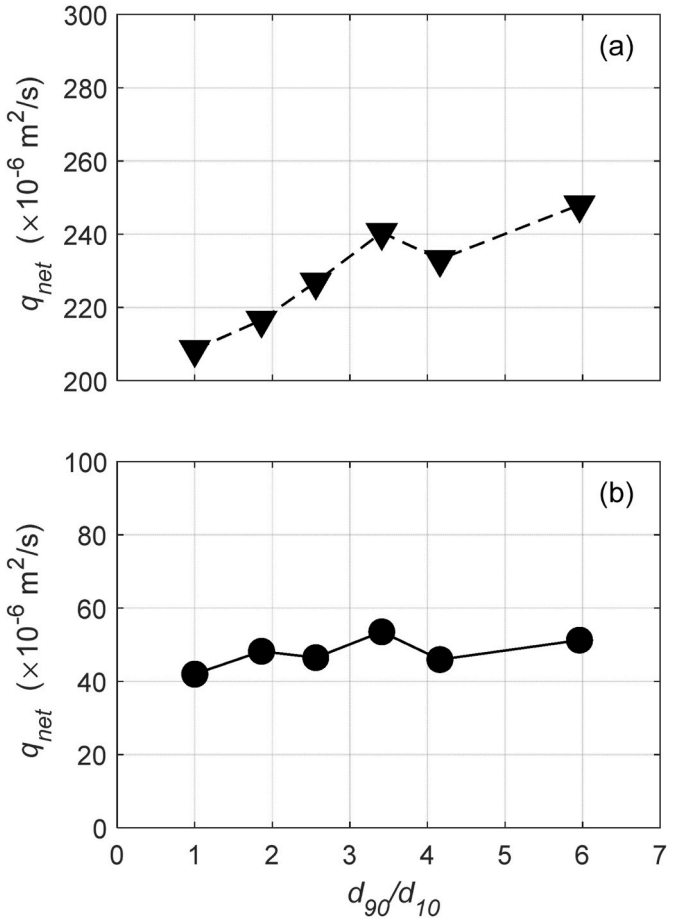


**Fig. 9.** Wave-period-averaged sediment transport rates for different size distributions represented by $d_{90}/d_{10}$ (see Table 2) under onshore velocity-skewed oscillatory flows of high ((a), I109R78B50) and low ((b), I88R63B50) velocity intensity.

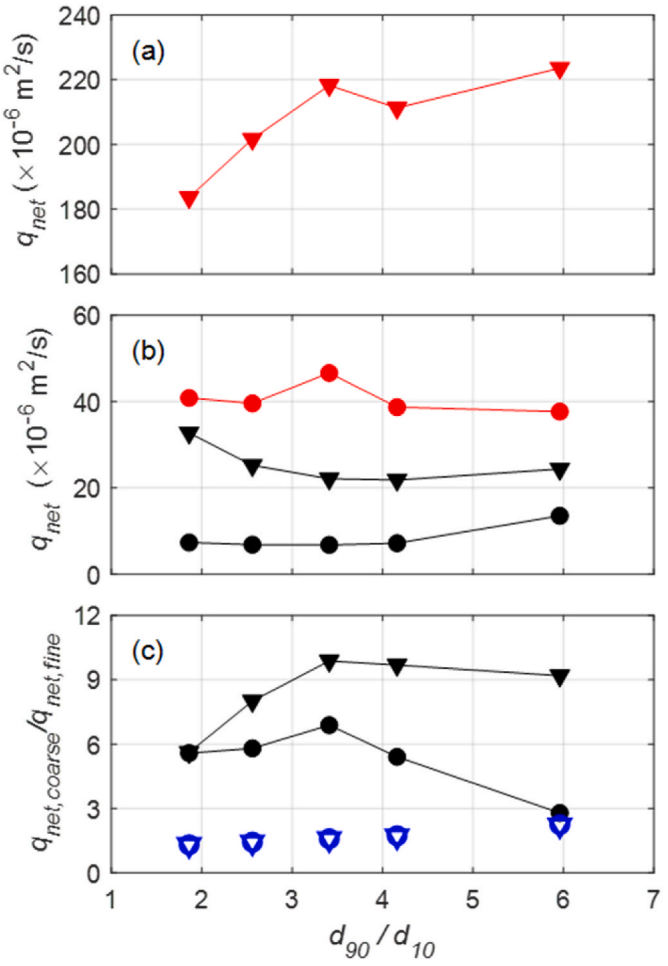


**Fig. 10.** (a, b) Model results of the wave-period-averaged transport rate corresponding to the coarse fraction ($d > d_{50}$, red symbols) and the fine fraction ($d < d_{50}$, black symbols) of different size distributions represented by their $d_{90}/d_{10}$ values under the oscillatory flows of low velocity intensity, I88R63B50 (circles), and high velocity intensity, I109R78B50 (triangles). (c) the ratio of the transported coarse fraction to the fine fraction corresponding to the flows I88R63B50 (circles), and I109R78B50 (triangles) as a function of $d_{90}/d_{10}$ values. The solid black symbols represent the model results and the open blue symbols represent the results calculated using the Van der A et al. (2013) parameterization. (For interpretation of the references to color in this figure legend, the reader is referred to the Web version of this article.)

ratio of the transported coarse particles to that of fine particles ($q_{net,\ coarse}/q_{net,\ fine}$) shown in Fig. 10 (c). It can be confirmed that under both flows with low and high velocity intensities, the total transport was dominated by the coarse particles (ratio greater than 3). Furthermore, the ratios are higher under higher velocity intensity (triangles in Fig. 10 (c)), which can be attributed to their deeper vertical sorting (compare Fig. 8 (b) and (c)). Intriguingly, the peak ratio (coarse to fine) corresponded to $d_{90}/d_{10} = 3.41$ (A3 distribution) under both low and high velocity intensities. When the size distribution of the graded sand bed is wider than a certain threshold, here shown to be $d_{90}/d_{10} = 3.41$, the contribution of the coarse fraction to the net transport rate starts to decrease as the mobility (particle velocity) of the very coarse sediment particles is reduced. Consequently, as the transport of coarse fraction reaches its peak, further widening the grain size distribution can no longer increase the net transport rate. Comparing the model results with the predictions using the Van der A et al. (2013) parameterization, it can be seen that although the parameterization predicted the net transport rate to be slightly dominated by the coarse fraction, it did not have the sensitivity to the flow velocity intensity (blue circles and triangles are almost on top of each other in Fig. 10 (c)). Furthermore, the monochromatic increment of $q_{net,\ coarse}/q_{net,\ fine}$ with the increasing $d_{90}/d_{10}$ was predicted by this parameterization. These behaviors can be attributed to the constant power of 0.25 that was used in the hiding/exposure factor in equation (14) such that $\varepsilon_{eff\,j}$coefficient depended only on the relative diameter of each size fraction to the median grain diameter.

In summary, model results show that the mobility (related to dimensional grain size and flow intensity) of the coarse grains in the bed surface layer plays a dominating role in the net transport. Since peak positive net transport rate occurs at $d_{90}/d_{10} = 3.41$, simulations to be presented in the remaining of the paper will focus on different oscillatory velocity shape scenarios using particle size distribution A3 ($d_{90}/d_{10} = 3.41$ see Table 2) and contrast the results with Uniform size distribution.

### 4.3. Gradation effects under velocity-skewed oscillatory flows

To further quantify the effect of size gradation on sediment transport driven by velocity-skewed flows, four additional flow conditions (I88R70B50, I88R78B50, I109R63B50, I109R70B50) to the ones discussed in Section 4.2, were also investigated (see Table 3). To emphasize the effect of size gradation under onshore velocity-skewed oscillatory flows, the ratio of wave-period-averaged (onshore) transport rate of the graded particles to that of the uniform particles ($q_{net,A3}/q_{net,\ Uniform}$) was plotted against the skewness parameter ($S_k$, see equation (17)) in Fig. 11. It can be seen that under all onshore velocity-skewed oscillatory flow conditions the size gradation effect increased the net onshore sediment

**Table 4**
Fractional and total transport rates for the simulated cases presented in Section 4.2 reported in $mm^2/s$.

| Flow ID | Distribution | Model | | | (Van der A et al., 2013) | | |
|---|---|---|---|---|---|---|---|
| | | $q_{net,\ coarse}$ | $q_{net,\ fine}$ | $q_{net}$ | $q_{net,\ coarse}$ | $q_{net,\ fine}$ | $q_{net}$ |
| I88R63B50 | Uniform | – | – | 41.9 | – | – | 66.6 |
| | A1 | 40.9 | 7.3 | 48.2 | 38.3 | 29.2 | 67.5 |
| | A2 | 39.6 | 6.8 | 46.4 | 40.6 | 28.3 | 68.9 |
| | A3 | 46.6 | 6.8 | 53.4 | 43.0 | 27.0 | 70.0 |
| | A4 | 38.7 | 7.2 | 45.9 | 45.3 | 26.0 | 71.3 |
| | BM | 37.7 | 13.5 | 51.2 | 58.9 | 26.2 | 85.1 |
| I109R78B50 | Uniform | – | – | 208.5 | – | – | 521.0 |
| | A1 | 183.6 | 32.7 | 216.3 | 298.7 | 229.0 | 527.7 |
| | A2 | 201.7 | 25.2 | 226.9 | 316.4 | 221.9 | 538.3 |
| | A3 | 218.3 | 22.1 | 240.4 | 335.7 | 212.1 | 547.8 |
| | A4 | 211.3 | 21.8 | 233.1 | 353.1 | 206.8 | 559.9 |
| | BM | 223.6 | 24.3 | 247.9 | 459.8 | 207.1 | 666.9 |

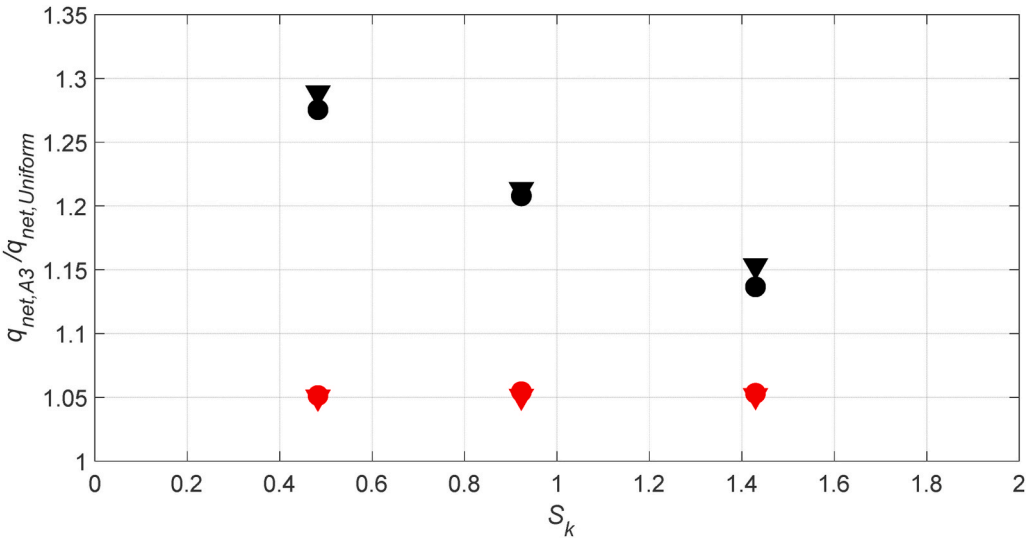


**Fig. 11.** The wave-period-averaged sediment transport rate ratio of the A3 to Uniform distributions (see Table 2) as a function of the skewness parameter ($S_k$) under onshore velocity-skewed oscillatory flows for present model results (black) and results using the Van der A et al. (2013) parameterization (red). Circles and triangles represent the oscillatory flows with $u_{rms}$ = 0.88 m/s and $u_{rms}$ = 1.09 m/s, respectively. (For interpretation of the references to color in this figure legend, the reader is referred to the Web version of this article.)

transport rate ($q_{net,A3}/q_{net,\ Uniform} > 1$) and the rate of increase dropped from 30% at low $S_k$ to about 15% in high $S_k$. It is also worth mentioning that by using $S_k$, which already used root-mean-square velocity to normalized the dimensional velocity skewness (see equation (17)), the ratio of $q_{net,A3}/q_{net,\ Uniform}$ was very close for low and high velocity intensities (see black circles and triangles in Fig. 11). Our model results suggest that skewness parameter $S_k$ is useful in parameterizing gradation effect. Here, we can see more clearly that although the Van der A et al. (2013) parameterization predicts increase of onshore transport rate caused by size gradation, the predicted rate of increase is almost the same (at about 5% level) regardless of skewness intensity $S_k$,.

Because net transport over the entire period is the summation of onshore (positive) transport during crest period and offshore (negative) transport during trough period, we examined the intra-wave transport features (Fig. 12) to illustrate how the vertical sorting effects (armoring and exposure) drove enhanced onshore transport under onshore velocity-skewed oscillatory flows. It can be seen that under the low velocity skewness (I88R63B50, Fig. 12 (b)), the instantaneous transport rates during the crest period were very close for the cases of graded (A3, red) and uniform (black) particles. Interestingly, during the trough period the instantaneous transport rate of the graded particles was notably lower than that of the uniform particles (compare the red and black lines within $0.4 < t/T < 1$ in Fig. 12 (b)). Results presented here suggested the dominance of armoring effect (flux reduction due to size gradation) during the trough period in which the flow intensity was generally lower than that during crest period. Fig. 12 (c) shows the time series of sediment transport rate of the graded and uniform particles driven by flow of high velocity skewness (I88R78B50). Similar to transport rate under low velocity skewness, we observed that during the crest period the instantaneous transport rate of graded and uniform particles are very close, while during the trough period the instantons transport rate of graded particles was lower than that of uniform particles. The main difference between the sediment transport rates under low (Fig. 12 (b)) and high (Fig. 12 (c)) velocity skewness was that during the trough interval, the reduction of offshore-directed (negative) transport rate due to armoring in graded case was more significant for low velocity skewness condition. This was at least partly because under higher velocity skewness (and the same root-mean-square velocity intensity), the trough flow intensity was already weaker (see Fig. 12(a)) and hence its contribution to reduce the positive transport during crest period was also weaker. This explains the trend observed in Fig. 11 that the increase in net onshore (positive) transport due to size gradation is larger for flow of lower velocity skewness.

More insights can be gained by comparing the sediment flux profiles averaged over the crest period and trough period. At the trough period, sediment flux throughout the entire profile for graded particles was smaller than that of uniform particles for both low and high velocity skewness cases (dash-dot lines in Fig. 12 (d) and (e)). The flow intensity in the trough was weaker and the mobility of coarse fraction in the sheet flow layer was lower while in the meantime, these coarse particles armored the fine fraction and further reduced suspended load. During the crest period under both flow conditions (solid lines in Fig. 12 (d) and (e)), the sediment flux of the graded particles was lower in the suspension layer due to armoring of the fine fraction. However, unlike the

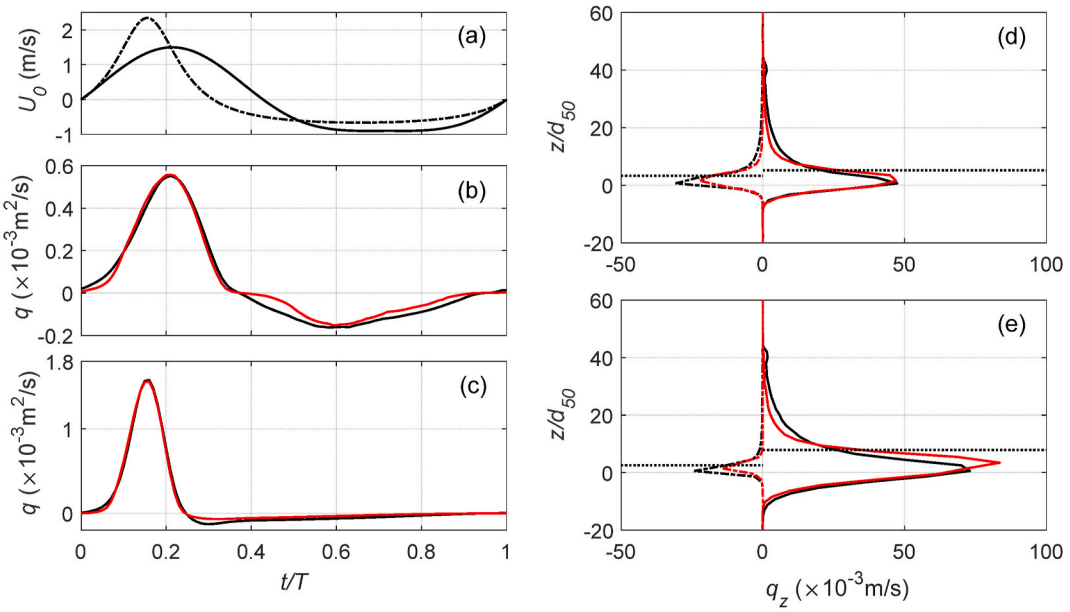


**Fig. 12.** (a) Time series of free stream velocity for low velocity skewness, I88R63B50 ($S_k = 0.48$, solid) and high velocity skewness, I88R78B50 ($S_k = 1.43$, dash-dot) conditions. Time series of sediment transport rate for Uniform (black) and A3 (red) size distributions under flows of low velocity skewness (b) and high velocity skewness (c). Time-averaged sediment flux profiles over the crest (positive) period (solid curves) and trough (negative) period (dash-dot curves) for Uniform (black) and A3 (red) size distributions for flows of low velocity skewness (d) and high velocity skewness (e). The elevation of volumetric sediment concentration of 0.08 is used to distinguish the suspension layer from the sheet flow layer (horizontal dotted lines). (For interpretation of the references to color in this figure legend, the reader is referred to the Web version of this article.)

trough period, sediment flux was consistently higher in the sheet flow layer due to exposure of the coarse fraction in more intense crest period. Moreover, during crest flows of both high and low velocity skewness, the flux reduction in suspension layer was more or less compensated by the flux enhancement in the sheet flow layer.

In summary, simulation results suggested that at the intra-wave timescale, increased/decreased sediment flux due to the exposure/armoring effect in the sheet flow/suspension layer co-exist and respond directly to the flow velocity intensity. Under low flow velocity intensity, particularly in trough interval, the armoring effect is dominant. As the flow velocity intensity increases during crest interval, the exposure effect in sheet flow layer may become more significant and competes with the armoring effect in the suspension layer. These processes result in enhanced onshore transport under onshore velocity-skewed oscillatory flows for graded sediments. For low velocity skewness condition, the reduction of transport (armoring) in trough interval in graded sediment is more significant than that for high velocity skewness condition (under the same RMS velocity intensity). Consequently, net onshore transport enhanced by grading effect is more significant at lower velocity skewness. Accordingly, the total transport is evidently influenced by a complex interplay of transport in the sheet flow layer (exposure) and suspension layer (armoring).

### 4.4. Gradation effects under acceleration-skewed oscillatory flows

To further investigate the effect of vertical sorting due to size gradation on sediment transport driven by onshore acceleration-skewed flows, six flow conditions were simulated with low and high values of velocity magnitude and acceleration skewness $\beta$ (see I92R50B62, I92R50B71, I92R50B78, I109R50B62, I109R50B71, I109R50B78 in Table 3). Notice that we intentionally selected wave conditions such that the velocity skewness was zero ($S_k = 0$, or $R = 0.5$) in order to evaluate solely the effect of acceleration skewness. The combined velocity and acceleration-skewed flows will be discussed later in Section 4.5.

To illustrate the intra-wave characteristics, Fig. 13 shows the results of the case I92R50B78 which corresponds to flow intensity $u_{rms} = 0.92$ m/s with high acceleration skewness ($\beta = 0.78$, $A_s = -0.64$). The armoring effect was dominant throughout the flow cycle, as the instantaneous transport rate of the graded particles (A3) was mostly lower (in magnitude) than that of the uniform particles (see Fig. 13(b)). Moreover, we can visually observe that the effect of armoring was more significant during the crest interval ($0 < t/T < 0.5$) as the transport rate reduction due to size gradation was greater especially during the maximum crest and deceleration ($0.1 < t/T < 0.4$). One can also notice onshore transport reduction in graded case during offshore-onshore flow reversal between $t/T = 0.97$ to $t/T = 0.04$. Because the reduction of transport induced by size gradation was more pronounced during crest interval, an overall 15% lower wave-period-averaged onshore (positive) transport rate for the graded particles was observed (see Table 5).

A better analysis on the effect of size gradation under onshore acceleration-skewed flows can be obtained by comparing the sediment flux profiles of graded (A3) and uniform particles (Fig. 13 (c)). At the maximum flow crest, the sediment flux enhancement due to size gradation in the sheet flow layer (below the horizontal dotted line) was 33 mm$^2$/s while the flux reduction in the suspension layer (above the horizontal dotted line) was 75 mm$^2$/s. Hence, the net positive flux was reduced by 42 mm$^2$/s due to grading via more significant reduction in suspension layer. On the other hand, at maximum flow trough the corresponding flux enhancement in the sheet flow layer was 53 mm$^2$/s (offshore-directed) versus flux reduction of 67 mm$^2$/s (offshore-directed) in the suspension layer. Hence, there was a net offshore flux reduction due to grading but only for 14 mm$^2$/s. The quantitative data shown here suggested that the armoring effect on suspended load was more pronounced during flow crest and led to reduction of onshore transport.

Another interesting feature we like to discuss is regarding the time series of sediment transport rates (Fig. 13 (b)) during the offshore-onshore flow reversal ($t/T = 0$) being significantly greater than zero (about $0.1 \times 10^{-3} m^2/s$). Notice that these values were significantly higher compared to those at onshore-offshore flow reversal ($t/T = 0.5$). This can be attributed to the phase lag effects due to a relatively short period of deceleration from the maximum flow trough ($t/T = 0.85$) to

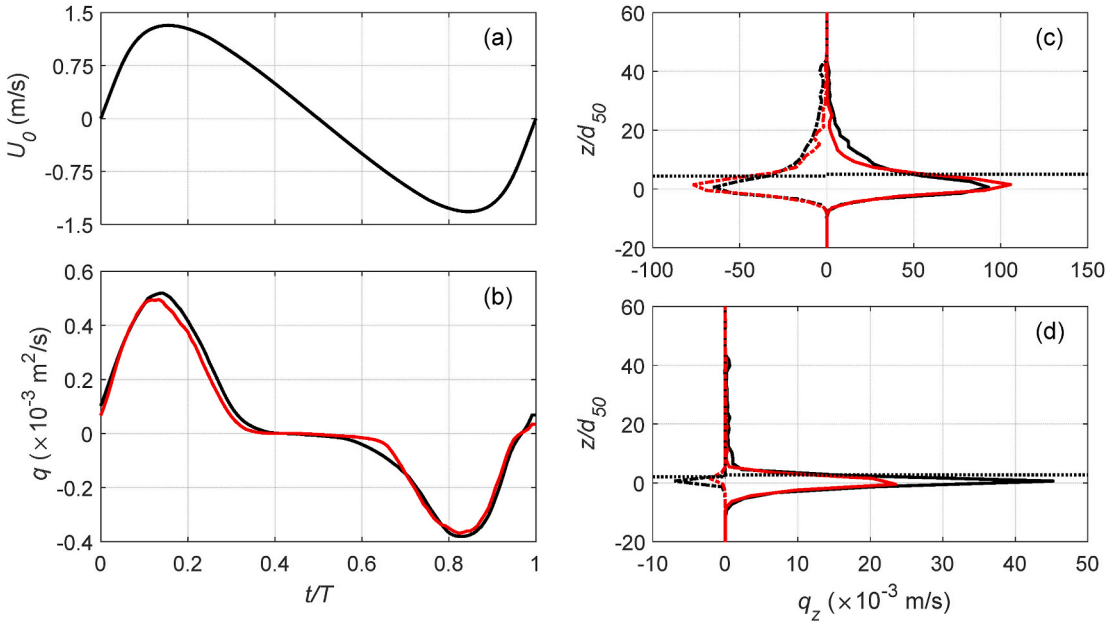


**Fig. 13.** (a) Time series of free-stream velocity for acceleration-skewed oscillatory flow with high asymmetry, I92R50B78 ($A_s$ = -0.64). (b) Time series of sediment transport rate for Uniform (black) and A3 (red) size distributions. (c) Sediment flux profiles corresponding to Uniform (black) and A3 size distributions (red) at the peak flow during crest (solid) and the peak flow during trough (dash-dot). (d) Sediment flux profiles at the offshore-onshore flow reversal ($t/T = 0$, solid) and at the onshore-offshore flow reversal ($t/T = 0.5$, dash-dot) for Uniform (black) and A3 (red) size distributions. The elevation of volumetric sediment concentration of 0.08 is used to distinguish the suspension layer from the sheet flow layer (horizontal dotted lines). (For interpretation of the references to color in this figure legend, the reader is referred to the Web version of this article.)

**Table 5**
Net sediment transport rates for the simulated cases presented in Section 4.3, 4.4 and 4.5 reported in mm$^2$/s.

| Flow ID | Model | | (Van der A et al., 2013) | |
|---|---|---|---|---|
| | Uniform | A3 | Uniform | A3 |
| I88R63B50 | 41.9 | 53.4 | 66.6 | 70.0 |
| I88R70B50 | 77.6 | 93.8 | 151.8 | 160.0 |
| I88R78B50 | 109.2 | 124.1 | 272.2 | 286.7 |
| I109R63B50 | 77.9 | 100.4 | 130.8 | 137.4 |
| I109R70B50 | 141.8 | 172.0 | 288.7 | 303.4 |
| I109R78B50 | 208.5 | 240.4 | 521.0 | 547.8 |
| I92R50B62 | 10.9 | 7.2 | 15.3 | 16.3 |
| I92R50B71 | 20.1 | 15.6 | 33.6 | 35.3 |
| I92R50B78 | 31.6 | 27.0 | 61.5 | 64.3 |
| I109R50B62 | 19.8 | 15.6 | 32.0 | 34.6 |
| I109R50B71 | 38.4 | 32.7 | 56.0 | 60.5 |
| I109R50B78 | 63.2 | 54.0 | 99.65 | 104 |
| I88R57B57 | 34.9 | 38.3 | 56.9 | 60.3 |
| I88R60B54 | 44.25 | 49.9 | 72.35 | 76.5 |
| I88R54B60 | 26.1 | 24.2 | 40.95 | 43.6 |

the flow reversal ($t/T = 1$), where the sediment particles suspended during flow trough period did not have enough time to completely settle back to the immobile bed (Dohmen-Janssen et al., 2002). Looking into the sediment flux profiles at flow reversals (13 (d)), it was evident that at the offshore-onshore flow reversal ($t/T = 0$, solid lines) the sediment fluxes were significantly higher than the sediment fluxes at the onshore-offshore flow reversal ($t/T = 0.5$, dash-dot lines). Our model results were consistent with laboratory studies reported by Ruessink et al. (2011) that phase-lag effect played a role in causing onshore transport under onshore acceleration-skewed flow because duration of offshore-onshore transition was shorter than that of onshore-offshore transition. However, we also need to point out that phase-lag effect was conventionally associated with suspended load quantified by a phase-lag parameter proposed based on relative timescales between wave period and particle settling time in the boundary layer (Dohmen-Janssen et al., 2002). For the present coarse sand condition, the phase-lag parameter obtained this way was about 0.01, which was significantly smaller than the critical value of 0.038 suggested by Dohmen-Janssen et al. (2002). Examining the model results further revealed that the sediment flux at $t/T = 0$ was mainly in the high concentration region (Fig. 13 (d), below the horizontal dotted line), suggesting that when sediment particles settled back to the bed, they first entered a mobile layer that remained relatively energetic and moving onshore due to the phase lead of bottom shear stress and particle collisions. Comparison of the flux profiles of the uniform and graded (A3) particles at $t/T = 0$ showed that the armoring was also effective at this instant since the onshore flux of the graded particles was considerably lower compared to the uniform particles. In summary, armoring of suspended sediment transport by the coarse fraction at flow crest period and phase-lag effect in conjunction with armoring effect during offshore-onshore flow reversal were the two main reasons causing reduced wave-period-averaged net onshore sediment transport under onshore acceleration-skewed flows in graded sediments. We like to emphasize that both reasons are directly related to the reduced fine fraction in suspended load due to armoring by the coarse fraction.

Fig. 14 shows the wave-averaged net sediment transport rate ratios between graded sediment cases (A3) and their uniform grain counterpart for all the onshore acceleration-skewed flows. The present model results indicated that size gradation reduced the net onshore sediment transport rate driven by onshore acceleration-skewed flows by 15–35%. Furthermore, the reduction of the net transport rate was higher under flows of low asymmetry parameter ($A_s$ = -0.25) and low velocity intensity ($u_{rms}$ = 0.92 m/s, black circles in Fig. 13). The more pronounced size gradation effect on the net transport rate under lower asymmetry and lower flow intensity was clearly due to the more significant armoring effects, namely, the coarse fraction was harder to get mobilize in low intensity flow and hence the fine fraction transported as suspended load is more significantly limited. On the other hand, during more intense and higher asymmetry flows, coarse fraction can be more easily mobilized, the armoring effect becomes weaker, and the onshore transport can be recovered closer to the uniform grain (no grading) condition. The Van der A et al. (2013) parameterization predicts an

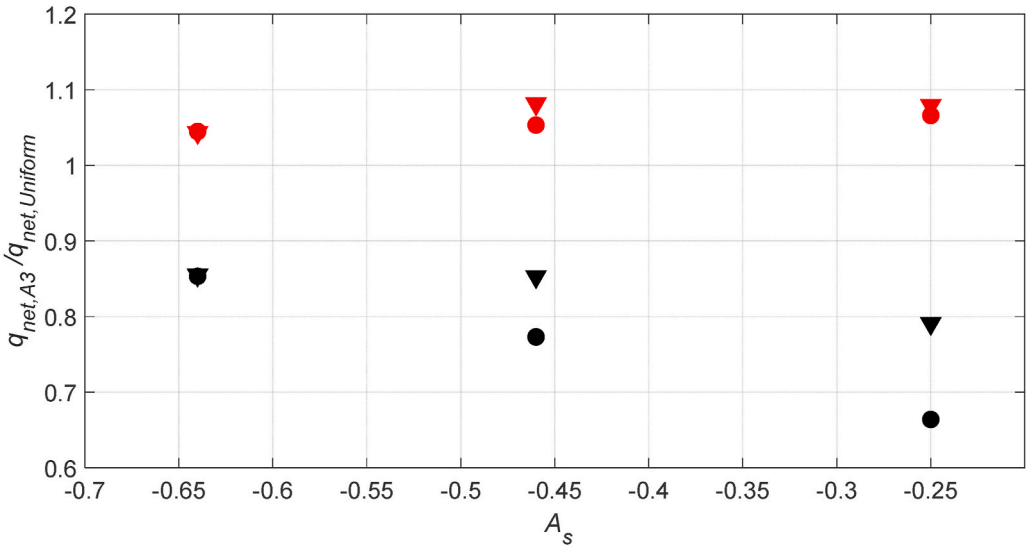


**Fig. 14.** The net transport rate ratio of the A3 to Uniform distributions (see Table 2) as a function asymmetry parameter ($A_s$) under onshore acceleration-skewed oscillatory flows for present model results (black) and results using the Van der A et al. (2013) parameterization (red). Circles and triangles represent the oscillatory flows with $u_{rms}$ = 0.92 m/s and $u_{rms}$ = 1.09 m/s, respectively. (For interpretation of the references to color in this figure legend, the reader is referred to the Web version of this article.)

increase of net onshore transport rate due to size gradation, which gives a trend similar to the prediction under onshore velocity-skewed oscillatory flow conditions.

### 4.5. Gradation effects under combined-skewed oscillatory flows

It is widely-accepted that near and after wave breaking, wave-driven flow velocity becomes onshore acceleration-skewed. However, as observed in the laboratory and field (e.g., Doering and Bowen, 1995; Elfrink et al., 2006; Mieras et al., 2019), nearshore breaking waves with only acceleration skewness and zero velocity skewness are scarce. Near the break point at the sandbar crest, near-breaking waves have both high onshore velocity skewness and onshore acceleration skewness (Elgar et al., 1988). As broken waves propagate landward, they become more developed bore with higher onshore acceleration skewness, while the velocity skewness decreases. On the other hand, pure onshore velocity-skewed waves may only exist offshore of the break point. Since waves observed in the surf zone often show combined acceleration skewness and velocity skewness, we performed simulations with three more flow conditions of combined velocity and acceleration skewness (I88R57B57, I88R60B54, and I88R54B60 in Table 3) for graded (A3) and uniform particle size distributions. To quantify the relative importance of velocity and acceleration skewness, the parameter $\varphi$ suggested by Abreu et al. (2010) was used in (19). When $\varphi$ = - 90°, a pure velocity-skewed wave is obtained, whereas $\varphi$ = 0° gives a pure acceleration-skewed wave.

Fig. 15 shows the relative net sediment transport rate of graded to uniform particles for combined onshore velocity-skewed and acceleration-skewed flows. To qualitatively relate our simulations to wave conditions in a typical surf zone, the horizontal axis of Fig. 15 roughly represents the seaward to landward transition (left to right) where the center portion (- 60° < $\varphi$ < - 30°) represents waves close to the breaking point. It can be seen that at large velocity skewness and low acceleration skewness ($\varphi$ closer to -90°, offshore of the break point), the relative net transport rate of graded to uniform particles increased up to about 1.3. The results demonstrated that as the onshore velocity skewness became dominant, the size gradation effect enhanced the onshore sediment transport rate. Moving toward the landward direction approaching the break point (- 60° < $\varphi$ < - 30°), the increased/decreased onshore transport due to grading effect reduced to only 10%. Landward

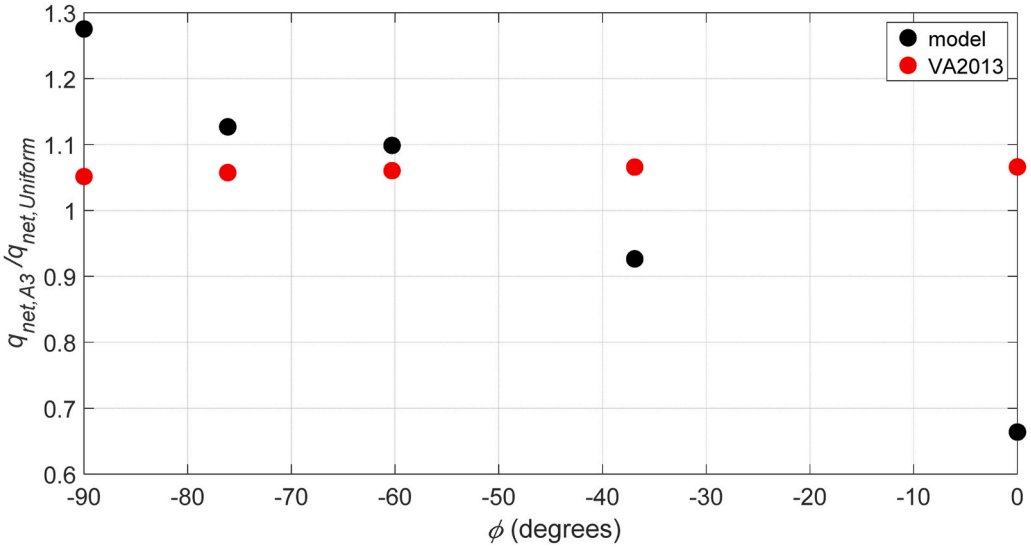


**Fig. 15.** The net transport rate ratio of the A3 to Uniform distributions (see Table 2) as a function of waveform parameter, $\varphi$, under combined onshore velocity and acceleration-skewed flow conditions for present model results (black) and results using the Van der A et al. (2013) parameterization (red).

of the breaking point when the acceleration skewness became dominant, grading effect decreased onshore transport down to about 30% when waves became purely acceleration skewed. Predictions based on the formula of Van der A et al. (2013) suggested a 5% increase in the net onshore transport rate due to size gradation regardless of the degree of velocity or acceleration skewness.

We like to point out that in this numerical experiment, the root-mean-square velocity intensity was maintained the same at different cross-shore locations for simplicity. In a real surf zone, wave intensity variability, in addition to wave shape variability, also plays an important role in cross-shore sediment transport. As a first step, our main goal is to identify the sediment size gradation effect due to wave shape variability in the cross-shore direction on beach profile evolution. Since cross-shore beach profile evolution required spatial gradients in the transport rate in the cross-shore direction, we can infer that the present numerical simulation results suggested size gradation plays a role in controlling beach profile evolution. In particular, grading effect may encourage accumulation of sediment near the break point due to wave shape transition from onshore-velocity skewed to onshore-acceleration skewed condition. A more extensive investigation on sediment size gradation effect on cross-shore sediment transport in a realistic surf zone should be carried out in the future.

## 5. Discussion

For mixed sediment environment, the active layer depth concept is often used to parameterize armoring effects on suspended sediment. Namely, the amount of bed sediment available for suspension must be limited by the active layer depth, which is controlled by the sediment transport state and the coarser fraction. Wiberg et al. (1994) and Harris and Wiberg (1997) proposed a semi-empirical formulation to parameterize active layer depth for ripple bed condition. In the present sheet flow condition, the active layer represents the effect of flow velocity intensity on mobilization and transport of particles in graded sediment bed. Based on the discussion in section 4.2, although the erosion depth may be slightly smaller than the active layer depth, it can serve as a surrogate for active layer depth in sheet flow. Here, we used the peak erosion depth under the oscillatory flow motion with instantaneous non-erodible bed defined by volumetric sediment concentration of 0.6. Fig. 16 depicts the maximum erosion depth corresponding to the graded (A3 distribution in Table 2) and uniform-sized particles for all the flow conditions simulated in the present work (Table 3) as a function of the peak Shields parameter $\theta_{max}$, which is defined as,

$$\theta_{max} = \frac{\tau_{b,max}}{(\rho_f - \rho_s) g d_{50}}. \tag{20}$$

The peak bottom shear stress $\tau_{b,max}$ for each case shown in Fig. 16 was calculated using the parameterization by Soulsby (1997) (see Appendix) which is very close (within 20% of difference) to the ones calculated directly from the model results using the eddy viscosity (Nielsen, 1992). Fig. 16 shows that the peak erosion depths corresponding to the graded particles (A3, red symbols) are about 15–35% smaller than those of the uniform-sized particles (black symbols). This can be attributed to the lower mobility of the fine fraction of graded particles in the deep bed layers due to the armoring effect.

There have been several parameterizations suggested to predict the peak erosion depth for sheet flows based on data obtained in oscillatory tunnel flow experiments (e.g., Flores and Sleath, 1998; O'Donoghue and Wright, 2004a). For instance, the parameterization suggested by Flores and Sleath (1998) calculates peak erosion depth as,

$$\frac{\delta_{e,max}}{d_{50}} = 3\theta_{max}. \tag{21}$$

As shown in Fig. 16, model results of graded particles (red symbols) agree reasonably well with this empirical formula (see dashed line) and in fact, better agreement can be achieved if we used lower sediment concentration (such as 0.55) to represent the non-erodible bed.

Harris and Wiberg (1997) suggested a parameterization to predict the active layer thickness $\delta_{mix}$ as a function of effective bed shear stress for ripple bed condition. In order to provide an active layer depth formula for sheet flow condition that is directly associated with peak erosion depth, we use a nondimensional form of the formula suggested by Harris and Wiberg (1997) which can be written as,

$$\frac{\delta_{mix}}{d_{50}} = k_1(\theta_{max} - \theta_{cr}) + k_2, \tag{22}$$

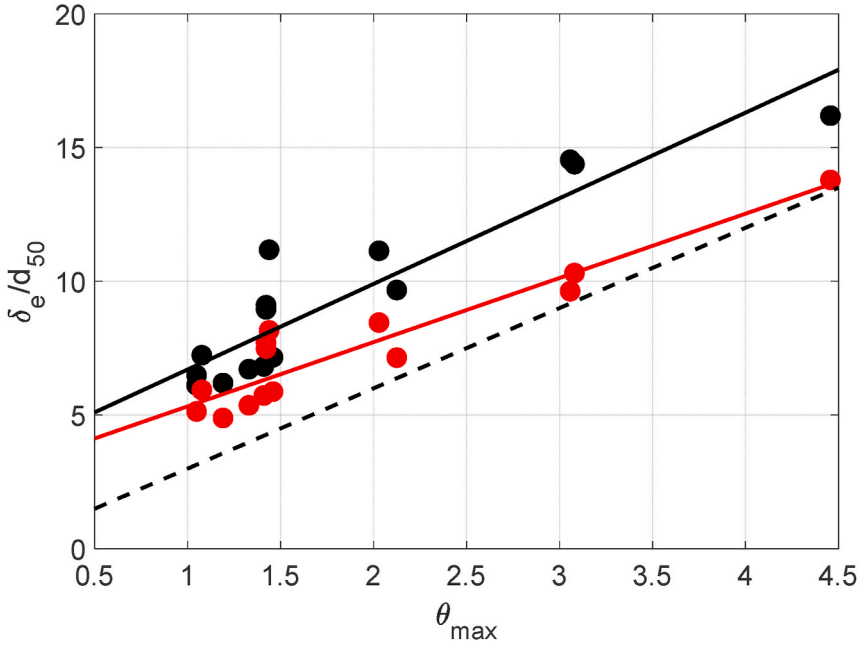


**Fig. 16.** Peak erosion depth as a function of maximum bed shear stress for Uniform (black symbols) and A3 (red symbols) size distributions (see Table 2). For comparison, erosion depth formula of Flores and Sleath (1998) (dashed line) and the calibrated formula for active layer depth of Harris and Wiberg (1997) for Uniform (solid black line) A3 (solid red line) size distributions for sheet flow condition are shown.

where $\theta_{cr}$is the critical Shields parameter (see Appendix), $k_1$and $k_2$are the calibration coefficients. Using (22), we calibrated the $k_1$and $k_2$to match with the model results of Uniform (solid black line) and A3 (solid red line) size distributions (Fig. 16, see Table 2). Model results show that the sediment size gradation reduces the active layer thickness as the layer thickness is 30% higher on average for the Uniform distribution than that of A3 distribution. Accordingly, the coefficients were obtained as $k_1 = 3.2$ and $k_2 = 3.6$ for Uniform distribution and as $k_1 = 2.4$ and $k_2 = 3.0$ for A3 size distribution. Results presented in Fig. 16 show a preliminary effort to quantify the active layer thickness in sheet flow condition, which can be used in the regional-scale hydrodynamic and morphodynamic models (e.g., Warner et al., 2010). More extensive simulations for different median grain size $d_{50}$ and wave condition are needed for a complete parameterization of active layer thickness in sheet flow condition.

## 6. Conclusion

The present Eulerian-Lagrangian numerical study of sheet flow sediment transport for coarse sand revealed that sediment size gradation influences the onshore sediment transport driven by onshore velocity-skewed and acceleration-skewed flows. Consistent with previous studies, simulations showed that inverse grading (upward coarsening) of sediment particles was generated during wave-driven transport, which was affected by the armoring and exposure effects. Simulations also demonstrated that the degree of size gradation affects the relative abundance of the coarse fraction in the transport. For transport driven by onshore velocity-skewed flows, largest increase of the net onshore sediment transport rate due to size gradation occurred when the coarse fraction ($d > d_{50}$) has the maximum contribution to the transport. Considerable widening the size distribution under the same flow velocity intensity may not increase the gradation effect on net transport rate as the mobility of coarse fraction may be hindered.

Simulations of sediment transport under oscillatory flow motion revealed a strong interplay between armoring and exposure effects in both the temporal evolution of transport and the vertical flux profiles between the sheet flow and suspended load layers. The present study revealed that size gradation led to inverse grading with coarse fraction armored the bed surface layer which limited the fine fraction. For coarse sand transport in typical nearshore flow intensity, reduction of transport rate due to armoring prevailed except for very high flow intensity. Consequently, more significant reduction of transport always occurred during trough period in onshore velocity-skewed flows and hence size gradation effect increased net onshore transport. Minor exposure effect can also occur during crest period under high velocity intensity which further increased onshore transport. Moreover, size gradation effect decreased net onshore transport for onshore acceleration-skewed flows due to more pronounced armoring effect during offshore-onshore flow reversal and the flow crest period. Overall, numerical model results revealed the dependence of grading effect on wave condition, namely velocity skewness, acceleration skewness and wave intensity while predictions using the parameterization of Van der A et al. (2013) did not show sensitivity to wave conditions.

The active layer depth concept was extended for sheet flow condition by associating it with the erosion depth. Model results was used to provide a preliminary view of an empirical formula for sheet flows extending the one provided by Harris and Wiberg (1997) for ripple bed condition. Our analyses provide insights into how size grading effect can influence wave-driven onshore sediment transport which is important to further predict morphodynamic evolution. However, the interplay between armoring and exposure in velocity-skewed and acceleration-skewed oscillatory flows may be different for medium and fine sands and future investigation is warranted.

## Declaration of competing interest

The authors declare that they have no known competing financial interests or personal relationships that could have appeared to influence the work reported in this paper.

## Acknowledgments

This study was supported by Office of Naval Research (N00014-18-1-2785) and National Science Foundation (OCE-1537231; OCE-1635151; OCE-1756714). Joseph Calantoni was supported under base funding to the U.S. Naval Research Laboratory from the Office of Naval Research. Numerical simulations presented in this study were carried out using the Farber and Caviness cluster at University of Delaware, and the SuperMic cluster at Louisiana State University via XSEDE (OCE100015).

## Appendix. Soulsby (1997) bottom shear stress parameterization

Soulsby (1997) calculated the bottom shear stress as,

$$\tau_b = \frac{1}{2}\rho f_w U_w^2, \tag{A.1}$$

where $f_w$is the wave friction factor and $U_w$is the orbital velocity amplitude. The wave friction factor is calculated following Swart (1974) and it is written as,

$$\begin{aligned} f_w &= 0.3 && r \le 1.57, \\ f_w &= 0.00251 exp(5.21 r^{-0.19}) && r > 1.57, \end{aligned} \tag{A.2}$$

where $r$is the relative roughness calculated as $r = A/k_s$, with $k_s$being the equivalent grain roughness estimated as $k_s = 2.5d_{50}$. $A$is the semi-orbital excursion calculated as,

$$A = \frac{U_w T}{2\pi}, \tag{A.3}$$

where $T$represents the wave period.

The critical Shields parameter is calculated as,

$$\theta_{cr} = \frac{0.3}{1 + 1.2D_*} + 0.055[1 - exp(-0.02D_*)], \tag{A.4}$$

in which $D_*$is the non-dimensional sediment diameter,

$$D_* = \left[\frac{g(s-1)}{\nu^2}\right]^{1/3} d_{50}. \quad (A.5)$$

with $\nu$representing the kinematic viscosity of water.

## References


Van der A, D.A., O'Donoghue, T., Ribberink, J.S., 2010. Measurements of sheet flow transport in acceleration-skewed oscillatory flow and comparison with practical formulations. Coast. Eng. 57 (3), 331–342. https://doi.org/10.1016/j.coastaleng.2009.11.006.

Van der A, D.A., Ribberink, J.S., Van der Werf, J.J., O'Donoghue, T., Buijsrogge, R.H., Kranenburg, W.M., 2013. Practical sand transport formula for non-breaking waves and currents. Coast. Eng. 76, 26–42. https://doi.org/10.1016/j.coastaleng.2013.01.007.

Abreu, T., Silva, P.A., Sancho, F., Temperville, A., 2010. Analytical approximate wave form for asymmetric waves. Coast. Eng. 57 (7), 656–667. https://doi.org/10.1016/j.coastaleng.2010.02.005.

Abreu, T., Michallet, H., Silva, P.A., Sancho, F., Van Der A, D.A., Ruessink, B.G., 2013. Bed shear stress under skewed and asymmetric oscillatory flows. Coast. Eng. 73, 1–10. https://doi.org/10.1016/j.coastaleng.2012.10.001.

Amoudry, L.O., 2014. Extension of k-ω turbulence closure to two-phase sediment transport modelling: application to oscillatory sheet flows. Adv. Water Resour. 72, 110–121. https://doi.org/10.1016/j.advwatres.2014.07.006.

Amoudry, L.O., Liu, P.L.F., 2010. Parameterization of near-bed processes under collinear wave and current flows from a two-phase sheet flow model. Continent. Shelf Res. 30 (13), 1403–1416. https://doi.org/10.1016/j.csr.2010.04.009.

Balachandar, S., Eaton, J.K., 2010. Turbulent dispersed multiphase flow. Annu. Rev. Fluid Mech. 42 (1), 111–133. https://doi.org/10.1146/annurev.fluid.010908.165243.

Calantoni, J., Thaxton, C.S., 2008. Simple power law for transport ratio with bimodal distributions of coarse sediments under waves. J. Geophys. Res.: Oceans 113 (C3), 1–11. https://doi.org/10.1029/2007JC004237.

Calantoni, J., Holland, K.T., Drake, T.G., 2004. Modelling sheet-flow sediment transport in wave-bottom boundary layers using discrete-element modelling. Phil. Trans. Roy. Soc. Lond. 362 https://doi.org/10.1098/rsta.2004.1427, 1987–2001. Series A.

Cheng, Z., Hsu, T.J., Calantoni, J., 2017. SedFoam: a multi-dimensional Eulerian two-phase model for sediment transport and its application to momentary bed failure. Coast. Eng. 119, 32–50. https://doi.org/10.1016/j.coastaleng.2016.08.007.

Cheng, Z., Chauchat, J., Hsu, T.J., Calantoni, J., 2018. Eddy interaction model for turbulent suspension in Reynolds-averaged Euler–Lagrange simulations of steady sheet flow. Adv. Water Resour. 111, 435–451. https://doi.org/10.1016/j.advwatres.2017.11.019.

Cundall, P.A., Strack, O.D.L., 1979. A discrete numerical model for granular assemblies. Geotechnique 29 (1), 47–65. https://doi.org/10.1680/geot.1979.29.1.47.

Dibajnia, M., Watanabe, A., 1996. A transport rate formula for mixed-size sands. In: Coastal Engineering Proceedings, pp. 3791–3804. https://doi.org/10.1061/9780784402429.293. Retrieved from.

Doering, J.C., Bowen, A.J., 1995. Parametrization of orbital velocity asymmetries of shoaling and breaking waves using bispectral analysis. Coast. Eng. 26, 15–33. https://doi.org/10.1016/0378-3839(95)00007-X.

Dohmen-Janssen, C.M., Kroekenstoel, D.F., Hassan, W.N., Ribberink, J.S., 2002. Phase lags in oscillatory sheet flow: experiments and bed load modelling. Coast. Eng. 46, 61–87. https://doi.org/10.1016/S0378-3839(02)00056-X.

Drake, G., Calantoni, J., 2001. Discrete particle model for sheet flow sediment transport in the nearshore. J. Geophys. Res. 106 (C9), 19859–19868. https://doi.org/10.1029/2000JC000611.

Elfrink, B., Hanes, D.M., Ruessink, B.G., 2006. Parameterization and simulation of near bed orbital velocities under irregular waves in shallow water. Coast. Eng. 53, 915–927. https://doi.org/10.1016/j.coastaleng.2006.06.002.

Elgar, S., Guza, R.T., Freilich, M.H., 1988. Eulerian measurements of horizontal accelerations in shoaling gravity waves. J. Geophys. Res. 93 (8), 9261–9269. https://doi.org/10.1029/JC093iC08p09261.

Fernández-Mora, A., Calvete, D., Falqués, A., De Swart, H.E., 2015. Onshore sandbar migration in the surf zone: new insights into the wave-induced sediment transport mechanisms. Geophys. Res. Lett. 42, 2869–2877. https://doi.org/10.1002/2014GL063004.

Finn, J.R., Li, M., Apte, S.V., 2016. Particle based modelling and simulation of natural sand dynamics in the wave bottom boundary layer. J. Fluid Mech. 796, 340–385. https://doi.org/10.1017/jfm.2016.246.

Flores, N.Z., Sleath, J.F.A., 1998. Mobile layer in oscillatory sheet flow. J. Geophys. Res.: Oceans 103 (C6), 12783–12793. https://doi.org/10.1029/98JC00691.

Folk, R.L., Ward, W.C., 1957. Brazoz River bar: a Study in the significance of grain size parameters. J. Sediment. Petrol. 27 (1), 3–26. https://doi.org/10.1306/74D70646-2B21-11D7-8648000102C1865D. Retrieved from.

Foster, D.L., Bowen, A.J., Holman, R.A., Natoo, P., 2006. Field evidence of pressure gradient induced incipient motion. J. Geophys. Res.: Oceans 111 (C05004), 1–8. https://doi.org/10.1029/2004JC002863.

Goff, J.A., Mayer, L.A., Traykovski, P., Buynevich, I., Wilkens, R., Raymond, R., et al., 2005. Detailed investigation of sorted bedforms, or "rippled scour depressions," within the Martha's Vineyard Coastal Observatory, Massachusetts. Continent. Shelf Res. 25, 461–484. https://doi.org/10.1016/j.csr.2004.09.019.

Goniva, C., Kloss, C., Deen, N.G., Kuipers, J.A.M., Pirker, S., 2012. Influence of rolling friction on single spout fluidized bed simulation. Particuology 10, 582–591. https://doi.org/10.1016/j.partic.2012.05.002.

Graham, D.I., James, P.W., 1996. Turbulent dispersion of particles using eddy interaction models. Int. J. Multiphas. Flow 22 (1), 157–175. https://doi.org/10.1016/0301-9322(95)00061-5.

Haider, A., Levenspiel, O., 1989. Drag coefficient and terminal velocity of spherical and nonspherical particles. Powder Technol. 58, 63–70. https://doi.org/10.1016/0032-5910(89)80008-7. Retrieved from.

Harada, E., Gotoh, H., Tsuruta, N., 2015. Vertical sorting process under oscillatory sheet flow condition by resolved discrete particle model. J. Hydraul. Res. 53 (3), 332–350. https://doi.org/10.1080/00221686.2014.994139.

Harris, C.K., Wiberg, P.L., 1997. Approaches to quantifying long-term continental shelf sediment transport with an example from the Northern California STRESS mid-shelf site. Continent. Shelf Res. 17 (11), 1389–1418. https://doi.org/10.1016/S0278-4343(97)00017-4.

Hassan, W.N., Ribberink, J.S., 2005. Transport processes of uniform and mixed sands in oscillatory sheet flow. Coast. Eng. 52, 745–770. https://doi.org/10.1016/j.coastaleng.2005.06.002.

Hoefel, F., Elgar, S., 2003. Wave-induced sediment transport and sandbar migration. Science 299, 1885–1887. https://doi.org/10.1126/science.1081448.

Holland, K.T., Elmore, P.A., 2008. A review of heterogeneous sediments in coastal environments. Earth Sci. Rev. 89, 116–134. https://doi.org/10.1016/j.earscirev.2008.03.003.

Hsu, T.J., Hanes, D.M., 2004. Effects of wave shape on sheet flow sediment transport. J. Geophys. Res.: Oceans 109 (C05025), 1–15. https://doi.org/10.1029/2003JC002075. Retrieved from.

Hsu, T.J., Elgar, S., Guza, R.T., 2006. Wave-induced sediment transport and onshore sandbar migration. Coast. Eng. 53, 817–824. https://doi.org/10.1016/j.coastaleng.2006.04.003.

Julien, P.Y., Lan, Y., Berthault, G., 1993. Experiments on stratification of hetergeneous sand mixtures. Bull. Soc. Geol. Fr. 164 (5), 649–660.

Kim, Y., Cheng, Z., Hsu, T.-J., Chauchat, J., 2018. A numerical study of sheet flow under monochromatic nonbreaking waves using a free surface resolving Eulerian two-phase flow model. J. Geophys. Res.: Oceans 123. https://doi.org/10.1029/2018JC013930.

Kim, Y., Mieras, R.S., Cheng, Z., Anderson, D., Hsu, T.J., Puleo, J.A., Cox, D., 2019. A numerical study of sheet flow driven by velocity and acceleration skewed near-breaking waves on a sandbar using SedWaveFoam. Coast. Eng. 152 https://doi.org/10.1016/j.coastaleng.2019.103526.

Kleinhans, M.G., van Rijn, L.C., 2002. Stochastic prediction of sediment transport in sand-gravel bed rivers. J. Hydraul. Eng. 128 (4), 412–425. https://doi.org/10.1061/(ASCE)0733-9429, 2002)128:4(412.

Kloss, C., Goniva, C., Hager, A., Amberger, S., Pirker, S., 2012. Models, algorithms and validation for opensource DEM and CFD-DEM. *Progress in computational fluid dynamics*. Int. J. 12 (2/3), 140–152. https://doi.org/10.1504/PCFD.2012.047457.

Kranenburg, W.M., Ribberink, J.S., Uittenbogaard, R.E., Hulscher, S.J.M.H., 2012. Net currents in the wave bottom boundary layer: on waveshape streaming and progressive wave streaming. J. Geophys. Res.: Earth Surface 117, 1–18. https://doi.org/10.1029/2011JF002070.

Kranenburg, W.M., Ribberink, J.S., Schretlen, J.J.L.M., Uittenbogaard, R.E., 2013. Sand transport beneath waves: the role of progressive wave streaming and other free surface effects. J. Geophys. Res.: Earth Surface 118, 122–139. https://doi.org/10.1029/2012JF002427.

Liu, D., Liu, X., Fu, X., 2018. LES-DEM simulations of sediment saltation in a rough-wall turbulent boundary layer. J. Hydraul. Res. https://doi.org/10.1080/00221686.2018.1509384.

Luding, S., 2008. Introduction to discrete element methods: basic of contact force models and how to perform the micro-macro transition to continuum theory. European Journal of Environmental and Civil Engineering 12 (7–8), 785–826. https://doi.org/10.1080/19648189.2008.9693050.

Lyne, V.D., Butman, B., Grant, W.D., 1990. Sediment movement along the U.S. east coast continental shelf-II. Modelling suspended sediment concentration and transport rate during storms. Continent. Shelf Res. 10 (5), 429–460. https://doi.org/10.1016/0278-4343(90)90049-R.

Machado, M., Moreira, P., Flores, P., Lankarani, H.M., 2012. Compliant contact force models in multibody dynamics: evolution of the Hertz contact theory. Mech. Mach. Theor. 53, 99–121. https://doi.org/10.1016/j.mechmachtheory.2012.02.010.

Madsen, O.S., 1974. Stability of a sand bed under breaking waves. In: Coastal Engineering Proceedings, pp. 776–794. https://doi.org/10.1061/9780872621138.048. Copenhagen, Denmark. Retrieved from.

Maurin, R., Chauchat, J., Chareyre, B., Frey, P., 2015. A minimal coupled fluid-discrete element model for bedload transport. Phys. Fluids 27 (11). https://doi.org/10.1063/1.4935703.

Mieras, R.S., Puleo, J.A., Anderson, D., Hsu, T.-J., Cox, D.T., Calantoni, J., 2019. Relative contributions of bed load and suspended load to sediment transport under skewed-asymmetric waves on a sandbar crest. J. Geophys. Res.: Oceans 124. https://doi.org/10.1029/2018jc014564.

Nielsen, P., 1992. Coastal Bottom Boundary Layers and Sediment Transport. World Scientific.

Nielsen, P., 2006. Sheet flow sediment transport under waves with acceleration skewness and boundary layer streaming. Coast. Eng. 53, 749–758. https://doi.org/10.1016/j.coastaleng.2006.03.006.

O'Donoghue, T., Wright, S., 2004a. Concentrations in oscillatory sheet flow for well sorted and graded sands. Coast. Eng. 50, 117–138. https://doi.org/10.1016/j.coastaleng.2003.09.004.

O'Donoghue, T., Wright, S., 2004b. Flow tunnel measurements of velocities and sand flux in oscillatory sheet flow for well-sorted and graded sands. Coast. Eng. 51, 1163–1184. https://doi.org/10.1016/j.coastaleng.2004.08.001.

Ribberink, J.S., Al-Salem, A.A., 1994. Sediment transport in oscillatory boundary layers in cases of rippled beds and sheet flow. J. Geophys. Res.: Oceans 99 (C6), 12707–12727. https://doi.org/10.1029/94JC00380.

Van Rijn, L.C., 2007. Unified view of sediment transport by currents and waves. III: graded Beds. J. Hydraul. Eng. 133 (7), 761–775. https://doi.org/10.1061/(ASCE)0733-9429. Retrieved from. 2007)133:7(761.

Roelvink, D., Reniers, A., Van Dongeren, A., Van Thiel de Vries, J., McCall, R., Lescinski, J., 2009. Modelling storm impacts on beaches, dunes and barrier islands. Coast. Eng. 56, 1133–1152. https://doi.org/10.1016/j.coastaleng.2009.08.006.

Rosato, A., Strandburg, K.J., Prinz, F., Swendsen, R.H., 1987. Why the Brazil nuts are on top: size segregation of particulate matter by shaking. Phys. Rev. Lett. 58, 1038–1040. https://doi.org/10.1103/PhysRevLett.58.1038.

Ruessink, B.G., Michallet, H., Abreu, T., Sancho, F., Van Der A, D.A., Van Der Werf, J.J., Silva, P.A., 2011. Observations of velocities, sand concentrations, and fluxes under velocity-asymmetric oscillatory flows. J. Geophys. Res. 116 https://doi.org/10.1029/2010JC006443.

Schmeeckle, M.W., 2014. Numerical simulation of turbulence and sediment transport of medium sand. J. Geophys. Res.: Earth Surface 119 (6), 1240–1262. https://doi.org/10.1002/2013JF002911.

Schwartz, R.K., Birkemeier, W.A., 2004. Sedimentology and morphodynamics of a barrier island shoreface related to engineering concerns, Outer Banks, NC, USA. Mar. Geol. 211, 215–255. https://doi.org/10.1016/j.margeo.2004.05.020.

Sistermans, P.G.J., 2002. Graded Sediment Transport by Non-breaking Waves and a Current. PhD Thesis. Delft University of Technology. http://resolver.tudelft.nl/uuid:a61234fe-a3d8-433e-9196-96a851324bf6.

Soulsby, R.L., 1997. Dynamics of Marine Sands. Thomas Telford Publications.

Stauble, D., 1992. Long-term Profile and Sediment Morphodynamics: Field Research Facility Case History. U.S Army Corps of Engineers, Vicksburg, Mississippi. Technical Report CERC-92-7.

Sun, R., Xiao, H., 2016. SediFoam: a general-purpose, open-source CFD-DEM solver for particle-laden flow with emphasis on sediment transport. Comput. Geosci. 89, 207–219. https://doi.org/10.1016/j.cageo.2016.01.011.

Sun, R., Xiao, H., Sun, H., 2017. Realistic representation of grain shapes in CFD–DEM simulations of sediment transport with a bonded-sphere approach. Adv. Water Resour. 107, 421–438. https://doi.org/10.1016/j.advwatres.2017.04.015.

Swart, D.H., 1974. Offshore Sediment Transport and Equilibrium Beach Profiles. Delft Hydraulics Labratory. http://resolver.tudelft.nl/uuid:057cb136-5f5b-484a-878d-5616fbaeda4e.

Warner, J.C., Armstrong, B., He, R., Zambon, J.B., 2010. Development of a coupled ocean-atmosphere-wave-sediment transport (COAWST) modeling system. Ocean Model. 35 (3), 230–244. https://doi.org/10.1016/j.ocemod.2010.07.010.

Watanabe, A., Sato, S., 2004. A sheet-flow transport rate formula for asymetric, forward-leaning waves and currents. In: Coastal Engineering Proceedings, pp. 1703–1714. https://doi.org/10.1142/9789812701916_0136. Retrieved from.

Wiberg, P.L., Drake, D.E., Cacchione, D.A., 1994. Sediment resuspension and bed armoring during high bottom stress events on the northern California inner continental shelf: measurements and predictions. Continent. Shelf Res. 14 (10/11), 1191–1219. https://doi.org/10.1016/0278-4343(94)90034-5.